# The effects of processing parameters on the morphology of organic solar cells

Delwin Tanto

Department of Chemical and Materials Engineering
The University of Auckland

28 February 2018

A thesis submitted in fulfilment of the requirements for the degree of Master of Engineering in Chemical and Materials Engineering, the University of Auckland, 2018. This thesis is for examination purposes only and is confidential to the examination process.

# Abstract

Organic solar cells (OSCs) are increasingly commercially relevant due to their ability to harvest renewable solar energy more economically than traditional inorganic solar cells; however, current OSCs fall short in terms of their efficiency and longevity. Studies have suggested that the performance of OSCs is strongly influenced by the molecular assembly within the active layer, and as a result, can be improved by manipulating the morphology through processing. In this study, we first investigated the effects of thermal annealing and compositions on the morphology of P3HT:PCBM films prepared from a good solvent. This is followed by an investigation of P3HT fibres which were fabricated by dissolving and precipitating different concentrations of polymer in a poor solvent. Optical microscopy, atomic force microscopy, x-ray diffraction and Fourier-transform infrared spectroscopy were used to analyse the films, while UV-Vis was used to analyse the solutions. We found that as-cast films, despite displaying minimal phase separation, exhibit some degree of crystallinity in the form of short P3HT ribbons. Thermally annealing the films resulted in increased crystallinity and the nucleation of PCBM aggregates at high PCBM loadings, signifying the partial miscibility of PCBM in P3HT. Although insensitive to PCBM loading in as-cast films, the crystallinity of P3HT in the annealed films was enhanced by the addition of PCBM up to a mass ratio of 1:1, at which the crystallinity significantly drops. It suggests the duality of PCBM behaviour in a P3HT:PCBM film: a nucleating agent at low loadings and a plasticiser at high loadings. Furthermore, the diffusion of PCBM to form aggregates was found to be temperature-dependent, with PCBM forming macroscopic 'fans' at high annealing temperature. Subsequently, the onset of nucleation and the rate of growth of P3HT fibres in solution were observed to be strongly influenced by the concentration of the polymer, hence allowing better control of P3HT crystal morphology. For the first time, we also observed the self-assembly of these fibres into fractal snowflake crystal aggregates upon annealing. Future work will examine how PCBM and doping affect the P3HT fibres in solution and in film.

# Acknowledgements

I would like to convey my deepest gratitude to my supervisor, Dr Alisyn Nedoma for her continuous support during my research. Through her knowledge, enthusiasm and patience, she steered me in the right direction whilst allowing this paper to be my own work.

I would also like to thank Peter Martin, Laura Liang, Dr Matthew Sidford, Raymond Hoffmann, Dr Alec Asadov, Dr Yiran An and Catherine Hobbis for the training on the instruments. Without their help and advice, this study could not have been successful.

I would also like to acknowledge Lal Busher Azad, Sesha Manuguri and Sina Sheikholeslami who have helped me willingly with their knowledge through countless discussions.

Not to mention all my colleagues, the technicians and the academics in the Chemical and Materials Engineering Department of the University of Auckland who have shared their experiences and supported me in completing this work.

Finally, I must express my most sincere gratitude to my parents for providing me with unfailing support and continuous encouragement throughout my study and through the process of researching and writing this thesis. This accomplishment would not have been possible without them.

# Contents

# List of Figures

# List of Tables

# Chapter 1

# Introduction

With an estimated 0.5 zettajoules of global energy consumption per year[1] in addition to the issues of security and sustainability, there is a growing need for a cheap and renewable energy source. Scientists have raised interest in alternative energy sources, such as wind, water, geothermal and solar energy. Focusing on the latter, it provides a clean, environmentally friendly and reliable source of energy. The total global energy consumption is meagre in comparison to the estimated amount of energy we can harvest from the sun if all capacity were to be maximised, which is about 730 zettajoules per year. However, the European Photovoltaic Industry Association[2] estimated that solar energy fulfils just below 1 percent of the total global energy demand. The figure is not surprising considering that current solar cells are costly, which is caused by the complex processing methods, creating a long payback time. To this date, much research has focused on methods to harvest the solar energy efficiently.

The development of solar cells started in 1883 when Charles Fritts constructed the first solar cell using gold-coated selenium based on the photovoltaic effect, discovered by Edmond Becquerel about half a century earlier. Since then, photovoltaic technology has progressed rapidly, from an understanding of device physics to the discovery of new suitable materials and novel device structures. In 1939, Russell Ohl discovered the p–n junction, which later served as the building block of most semiconductor electronic devices. Ultimately, in 1954, Bell Labs managed to build the first practical silicon solar cell with an efficiency of about 6 percent. Four years later, the solar cell gained prominence after Vanguard I, the first solar-powered satellite, was launched by the U.S. Navy. Afterwards, scientists have managed to improve the efficiency of solar cells and utilise the technology for other applications, such as solar-powered buildings and calculators. Currently, the highest record of solar cell efficiency is held by a multi-junction solar cell, developed through a collaboration of Soitec, CEA-Leti and Fraunhofer Institute for Solar Energy Systems, at 46 percent efficiency[3].

Most of the existing solar cells are costly because they are manufactured from monocrystalline silicon. Moreover, the solar cell can only convert the light coming directly into the material. Therefore, the solar cell must be placed at a position such that it faces the sun the whole time to harvest as much energy as possible, something that is hard to achieve with rigid silicon-based solar cells. Those disadvantages of silicon-based photovoltaics inspired the

discovery of alternative materials for the solar cell, including conducting polymers and fullerenes.

The discovery of conducting polymer, the basis of organic solar cells, dated back to the mid-19$^{th}$ century, when Dr Henry Letheby observed the change in colour of aniline from blue-green to colourless when it was reduced and back to blue-green when it was oxidised[4]. However, it was not until the 1970s, when the conductivity of polymers was truly studied. Shirakawa *et al.*[5] investigated polyacetylene, which gives high electrical conductivity. Consequently, Shirakawa, MacDiarmid and Heeger were awarded the Nobel Prize in Chemistry in 2000 for their contributions to the discovery and development of conducting polymers.

While photovoltaic devices with organic dyes have been investigated since the 1950s, the first study of polymer in photovoltaic cells took place in 1980s. A breakthrough occurred when Tang[6] brought two different organic semiconductors together to give rise to an organic solar cell with 1 percent power conversion efficiency. One of the materials is called the donor–referring to its ability to provide electrons–and the other is called the acceptor–indicating its ability to accept electrons. The concept has since been employed in another combination of donor-acceptor materials, including polymer-polymer and polymer-fullerene blends. The latter has particularly received intense scrutiny due to the high electron affinity of fullerene, and therefore the blend's potential to convert solar energy with higher efficiency[7,8]. Presently, the most studied polymer-fullerene system is the poly(3-hexylthiophene) and [6,6]-phenyl-$C_{61}$-butryic acid methyl ester (P3HT:PCBM) due to its efficiency being superior to most of the other polymer-fullerene blends[9]. The P3HT:PCBM blend obtains its high efficiency from having their energy bands closer to one another, thus reduces charge recombination. Their mechanical properties, a wide range of electrical properties coupled with ease of processing have made the conducting polymers an attractive material for photovoltaic applications.

Despite that, the highest power conversion efficiency achieved for P3HT:PCBM photovoltaics to date is just over 6.5 percent[10,11]. Scharber and Sariciftci[12] calculated the maximum theoretical conversion efficiency of organic photovoltaics to be in the range of 15 to 16 percent. It clearly suggests that there is a lot of room for improvement before the power conversion efficiency of the organic photovoltaics saturates.

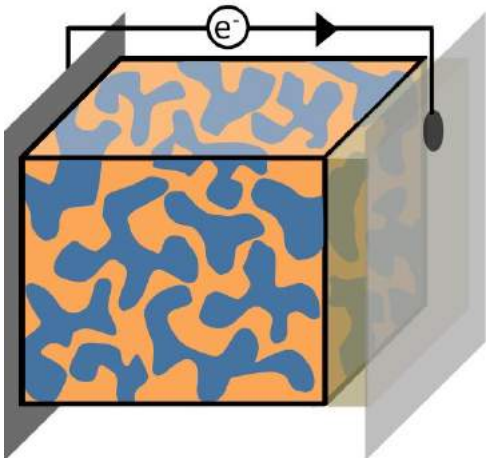


**Figure 1.1:** A schematic of a bulk heterojunction solar cell.

One of the underlying elements that determine the performance of organic photovoltaics is the morphology of the interface between the semiconductors. To understand how the morphology influences the performance of organic solar cells, it is important to look at the device physics first. Fundamentally, an exciton is generated when a photon with a sufficiently high energy impinges on the donor material. The exciton diffuses to the donor-acceptor interface and dissociates, resulting in charge transport to the electrodes to generate electrical energy. However, the exciton has a lifetime of about 50 picoseconds (1 picosecond is equivalent to $10^{-12}$ seconds), which means that the electron-hole pair will recombine and not induce any current if it does not reach the donor-acceptor interface in time [13,14]. Yu and Heeger [15] developed polymer composite bulk heterojunction photovoltaics, where the donor and acceptor materials form an interpenetrating network (Figure 1.1). It effectively increases the donor-acceptor interface area available for charge separation and shortens the distance the excitons have to diffuse through to reach the interface. In addition to the exciton dissociation, the microstructure of the materials also affects the subsequent charge transport from the interface to the electrode. The materials must provide continuous paths for the charge carriers to diffuse to the electrode and high charge carrier mobility, both of which are heavily influenced by the processing of the materials.

Therefore, it is of paramount importance to control the morphology of the organic solar photovoltaics with regard to obtaining a device with at least 10 percent power conversion efficiency, which is predicted to be the performance threshold for commercial viability. Yet, much of the work thus far has largely centred on improving the chemistry and measuring the performance of organic solar cells. This work will try to bridge between the chemistry and physics of organic solar cells as we strive to understand the effects of processing on their structure and properties.

# Chapter 2

# Literature Review

## 2.1 Organic solar cell

Brabec *et al.*[16] defined organic photovoltaics as solar cells that contain at least one organic semiconductor in the active layer, such as conjugated polymers, fullerenes and dyes. Organic semiconductors are of interest as photovoltaic materials owing to their high absorption coefficients, flexibility, light weight and low-cost processing[17,18].

Similar to a silicon solar cell, the most basic organic solar cell consists of electrodes and an active layer. The anode is usually made out of a high work function transparent conductive oxide, such as the indium tin oxide to allow light to penetrate and reach the active layer; the cathode is usually made out of a low work function metal, such as aluminium or calcium[19]. However, a typical organic photovoltaic device configuration also comprises an interlayer between the transparent anode and the light absorbing layer to minimise shunts. The interlayer is most commonly made out of poly(3,4-ethylenedioxythiophene):polystyrene sulfonate (PEDOT:PSS). In addition to reducing shunts, this interlayer improves the performance of the solar cell through increased anode selectivity of charge carriers[20], increased contact between the electrode and the active layer[21] as well as higher photovoltage through enrichment of polystyrene sulfonate components[22]. The active layer, however, plays the most important part in determining the performance of the solar cells because it is where the charge excitation and transport take place[23].

The light absorbing layer generally consists of a donor and acceptor material. Its morphology followed the work of Yu *et al.*[24], in which the donor and acceptor materials form a bi-continuous structure. The bulk heterojunction film can be prepared through melting the donor and acceptor materials Kim *et al.*[25] or solution processing where the donor and acceptor materials are intermixed in a solution before being deposited on a substrate, allowing for the development of cheap yet highly efficient organic solar cells. As an example, Park *et al.*[26] successfully employed the bulk heterojunction architecture to fabricate an organic solar cell with an internal quantum efficiency of close to 100%.

Among the organic materials for photovoltaic applications, polymer-fullerene solar

cells have seen a notably, if not the most, rapid progress during the past several years[16]. The fullerenes are exceptional electron acceptors in comparison to the conjugated polymers (as in polymer-polymer solar cells) and the inclusion of the fullerenes in a solar cell active layer greatly improves the performance of the device[7]. At the moment, the most studied polymer-fullerene cells are the poly(3-hexylthiophene-2,5-diyl):[6,6]-phenyl-$C_{61}$-butyric acid methyl ester (P3HT:PCBM)[9]. First investigated by Schilinsky *et al.*[27], the P3HT:PCBM blend is of great interest due to its high charge carrier mobility, good solubility and low bandgap.

## 2.2 Device physics

The organic solar cell operates on a similar principle as the inorganic solar cell. Upon the absorption of a photon, an electron in the highest occupied molecular orbital (HOMO) of the organic semiconductor is excited to the lowest unoccupied molecular orbital (LUMO). The HOMO and LUMO of organic semiconductors are analogous to the valence band and conduction band of the inorganic counterpart. However, in an organic solar cell, the electron-hole pair is coulombically bound due to the low dielectric constant and the localised charge carriers' wave function of the material[28]. This electron-hole pair is called an exciton and has a binding energy of 0.1–1.4 eV[29].

It is important to mention that Tang[6] successfully improved the performance of organic solar cells using two organic semiconductors which had their band levels correctly aligned. The requirements are that the HOMO and LUMO of the donor have to be higher than the HOMO and LUMO of the acceptor, respectively; and the difference between the HOMO of the donor and the LUMO of the acceptor has to be lower than the potential difference between the electron-hole pair[30]. After being generated, the exciton diffuses through the semiconductor toward the junction, irrespective of whether it is a linear junction or a heterojunction. Since the potential difference between the HOMO of the donor and the LUMO of the acceptor is lower than that of the exciton, the electron is transferred from the LUMO of the donor to the LUMO of the acceptor, while the hole remains in the HOMO of the donor. A partially dissociated exciton is also known as a geminate pair.

Subsequently, the drift and diffusion currents drive the geminate pairs toward the bulk heterojunction interface[31]. The difference between the work functions of the electrodes, which depend on the materials the electrodes are made from, generates an electric field within which the charge carriers drift along toward the electrodes, the first driving force. The concentration gradient of the charge carriers within the semiconductors induces the second driving force, the diffusion current of carriers. Since the concentration of charge carriers is higher close to the junction, the carriers diffuse away from the junction. Once the charge carriers are transported to the active layer/electrode interface, they are collected by the electrodes.

## 2.3 Active layer materials

Currently, the active layer of most high performance organic solar cells is based on a blend of a conducting polymer and a fullerene. The prerequisites to achieving high performance organic solar cells are that the donor polymer absorbs light with high efficiency and that there is a sufficient energy difference between the HOMO of the polymer and the LUMO of the fullerene. Hence, the ideal donor polymer should have a narrow bandgap and a low HOMO energy level, such are demonstrated by thiophene-based conducting polymers.

Thiophene-based conducting polymers, such as P3HT (Figure 2.1a), are typically selected as the donor material in the active layer because of their high absorption coefficient, allowing a very thin film of conducting polymers to absorb most of the light at their peak absorption wavelength[32]. This is the result of their backbones being less sterically hindered, thus leading to a more planar structure and a lower bandgap. Moreover, the properties of the P3HT can be further altered by changing its regioregularity. Highly regioregular P3HT is excellent for photovoltaic applications since it has an even lower bandgap[33], higher charge carrier mobility, broader absorbance spectrum and greater solubility, while also enabling for the formation of highly ordered P3HT crystals[34].

P3HT has side chains which make this polymer soluble in common organic solvents. They allow these conducting polymers to be cast from solution through wet processing techniques such as drop-casting, spin-coating, bar-coating and inkjet printing, which can be performed at ambient conditions at a low cost. The side chains also, to some extent, control the orientation and the electronic interaction between polymer chains[35].

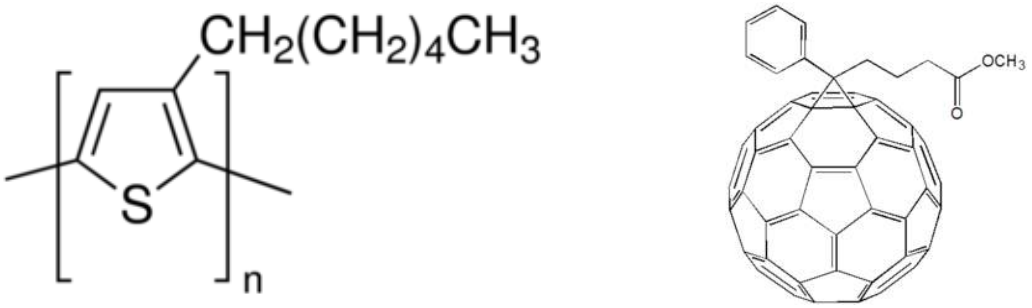


**(a)** **(b)**

**Figure 2.1:** (a) poly(3-hexylthiophene-2,5-diyl) (P3HT) molecule; (b) [6,6]-phenyl-$C_{61}$-butyric acid methyl ester (PCBM) molecule

The second component of the active layer material is the fullerene. As demonstrated by Kraabel *et al.*[36], when coupled with conjugated polymers, fullerene derivatives exhibit ultrafast photo-induced electron transfer. Fullerene derivatives, such as PCBM (Figure 2.1b), have been successfully used as electron acceptors in organic solar cells due to their high electron affinity and mobility[37]. The spherical shape of fullerene molecules means that they are isotropic electron acceptors and are excellent for bulk heterojunctions[38]. In addition, the bandgap of

most donor polymers, including P3HT, is smaller than that of fullerene derivatives, the HOMO energy levels of the fullerene are sufficiently low for efficient hole transfer from the acceptor to the donor. Another important characteristic of the fullerene derivatives is its relatively high dielectric constant, which mitigates charge recombination during device operation[39].

Out of all fullerene derivatives, PCBM has particularly been the subject of much research due to its phenyl moiety being small, hence making the molecule not much larger than the fullerene itself. However, the addition of that moiety has significantly improved the solubility, while maintaining the properties of the fullerene, such as the electron mobility and the dielectric constant[40]. The high solubility of PCBM ensures adequate mixing of polymer and fullerene to create a desired three-dimensional structure of the bulk heterojunction[41].

Although early works described the P3HT:PCBM bulk heterojunction as a binary system, Kiel *et al.*[42] indicated that the morphology is comprised of more than two pure domains. Parnell *et al.*[43] confirmed that statement by observing three distinct phases within the P3HT:PCBM thin layer, the crystalline P3HT, crystalline PCBM and a mixed phase of amorphous P3HT and PCBM, all of which are more defined upon thermal annealing.

P3HT and PCBM make a good polymer-fullerene combination for photovoltaic applications because they display similarly high solubility in an organic solvent such as chlorobenzene. A study by Troshin *et al.*[44], in which they compared the performance of P3HT devices with different fullerene derivatives, observed that P3HT:PCBM demonstrates one of the highest power conversion efficiency, surpassed only by P3HT with phenyl-$C_{71}$-butyric acid methyl ester ($PC_{71}BM$). The authors found that the morphology of the bulk heterojunction, therefore the performance, is best when the solubility of the acceptor material matches that of the donor material, which is the case for P3HT:PCBM photovoltaics.

## 2.4 Morphology versus processing parameters

As mentioned above, it has been reported that the performance of a bulk heterojunction solar cell is strongly associated with its morphology. Issues such as the short exciton's diffusion length and current-limiting space charge regions predominantly arise due to non-ideal microstructure of the active layer[14,45,46]. Therefore, it is critical to control the morphology of the P3HT:PCBM film to obtain a high-performing organic solar cell. Pre-deposition processing methods, such as using co-solvent[47,48], nucleating agent[49,50] and preforming P3HT fibres[51,52], as well as post-deposition processing methods, such as thermal annealing[53], solvent annealing[54–56] and supercritical carbon dioxide annealing[57,58], have been proposed to improve the performance of P3HT:PCBM solar cells.

## 2.5 Thermal annealing

Padinger *et al.*[53] proposed a post-deposition heat treatment method to improve the performance of P3HT:PCBM solar cells, in which the polymer-fullerene blends were subjected to both elevated temperature and an external electric field. This technique is only effective when the annealing temperature is above the blend's glass transition temperature, which is about 50°C for a 1:1 mass ratio P3HT:PCBM blend[59]. The same authors did not detect any significant change in the device's performance when annealed below this temperature.

Thermal annealing increases the power conversion efficiency of the devices due to the crystallisation of the P3HT to crystalline nanowires, which facilitates better charge transport within the active layer[60,61], and, to some extent, the aggregation of PCBM molecules, which forms percolation paths that improve the generated photocurrent[62]. The annealing was also found to coarsen the surface of the active layer, which effectively increases the interface area between the active layer and the electrode and improves the efficiency. A study by Treat *et al.*[63] found that the PCBM aggregates have little influence on the number and size of P3HT crystallites during thermal annealing. Rather, they are both miscible and mobile in amorphous P3HT, indicating that the PCBM phase aggregates and is dispersed in the amorphous P3HT region.

The resulting morphology of P3HT:PCBM blends upon heat treatment is strongly influenced by the annealing temperature and time. Motaung *et al.*[64] found that, for a specified annealing time, the crystallinity increases with annealing temperature. However, annealing the blends above 150°C leads to a slight disordering of P3HT crystallites. Similarly, prolonged annealing was found to soften the P3HT chains, which promotes the diffusion of PCBM particles through the amorphous P3HT, therefore greater phase separation[65]. Motaung *et al.*[66] also reported thermal decomposition of P3HT molecules, including the detachment of C–S units and $C_6H_{13}$ from the polymer backbone, upon extremely long annealing.

In extreme annealing conditions, those are high annealing temperature and long annealing time, the PCBM particles form micrometre-sized PCBM 'islands', which decrease the number of interconnected pathways for charge carriers to diffuse through and thus, the overall electron mobility within the active layer[67]. Since the surface energy of PCBM is higher than P3HT, Watts *et al.*[65] suggested that the driving force of this aggregation of PCBM molecules is the minimisation of surface energy. With increasing phase separation, the size of the domains grows larger than the exciton diffusion length, and therefore reduces the efficiency of the device. At intensely long thermal annealing, practically all PCBM molecules diffuse out of the P3HT, leaving behind a nearly pure and highly crystalline P3HT[68]. Large PCBM aggregates were also found to induce mechanical stress to the device which damages the polymer-fullerene interface, resulting in efficiency loss[62]. The degradation of the performance of a P3HT:PCBM solar cell can be described with an Arrhenius-type dependence with temperature[69].

Apart from the annealing temperature and time, there are several factors which influence

the post-annealing morphology of P3HT:PCBM thin films, such as the composition and the solid loading in solvent.

### 2.5.1 Composition

Müller *et al.*[70] argued that the P3HT:PCBM blend features eutectic phase behaviour. Both the morphology and the performance of the blend are dependent on its composition and the rate of solidification. The authors figured out the eutectic point of the P3HT:PCBM blend, the point where both of the components solidify from a homogeneous liquid mixture below the eutectic temperature at the same time, to be approximately 65 wt% P3HT (or 35 wt% PCBM).

Subsequently, they discovered that PCBM has a miscibility limit of about 40 wt% in P3HT. Their findings were supported by Chirvase *et al.*[62] who observed large PCBM aggregates when the miscibility limit is surpassed. The authors also found that the size and density of PCBM aggregates increase with PCBM loading. It is thought that, although high PCBM concentration produces large aggregates which are detrimental to the device's performance, a PCBM concentration below the miscibility limit does not provide good electron transport pathways.

### 2.5.2 Solid loading

The concentration of the polymer-fullerene solids dissolved within a solvent strongly influences the thickness of the films produced. Consequently, the morphology of the resulting polymer-fullerene films is controlled by the viscosity of the solution that is deposited.

van Bavel *et al.*[71] investigated the morphology of thermally annealed P3HT:PCBM films across different film thickness. They discovered that P3HT nanowires were visible on the top surface of thin films only, even though transmission electron microscope (TEM) indicated that there were P3HT crystallites in thick films as well. Additionally, they discovered that, in thin films, there was a density gradient of P3HT crystals across the thickness, with more P3HT nanowires near the bottom of the films. However, this vertical segregation of P3HT crystals was imperceptible in thick films, with crystalline P3HT distributed homogeneously across the thickness of the films. Therefore, it can be concluded that the kinetics of film transformations during film deposition and thermal annealing are not the same for different film thickness.

Sirringhaus *et al.*[72] attributed this difference in morphology as the effect of different solvent drying rate. Slow drying rate allows the P3HT molecules to form strong inter-chain interactions before the solvent evaporates. The PCBM molecules, on the other hand, are less dependent on the drying rate, demonstrated by a small change of the PCBM peak in the absorption spectra.

## 2.6 Preformed P3HT fibres

Berson *et al.*[51] developed a method to improve the morphology of P3HT:PCBM films through preforming P3HT nanofibres. Long P3HT nanofibres were fabricated by dissolving the polymer in a heated p-xylene, followed by cooling the solution down. After that, the P3HT fibres were separated from the dissolved P3HT solution through centrifugation and filtration. Thin films produced from a solution containing P3HT fibres, amorphous P3HT and PCBM displayed higher degree of P3HT crystallinity than thermally annealed amorphous P3HT and PCBM films without substantial fullerene aggregation.

Liu *et al.*[73] investigated the mechanism of P3HT crystallisation in solution and discovered that the process is initiated by the crystallisation of polymer chains into one-dimensional lamellar crystals, which is followed by chain folding through $\pi$–$\pi$ interactions within the polymer backbones. The length of the crystal fold is dependent on the temperature of the crystallisation. These lamellar crystals were found to evolve into two-dimensional ribbons at high P3HT concentration through a combination of $\pi$–$\pi$ stacking and alkyl chain interactions.

Subsequently, several other techniques have been proposed to fabricate similar P3HT fibres, such as using binary solvent mixture[74–76], ultrasonication[77] and directional solidification[78,79]. Altogether, preforming P3HT crystals enables fine control of both the crystalline content and the crystal dimension of P3HT in the solution and film.

## 2.7 Research gap

Unfortunately, the majority of studies have fixed their focus on improving the performance of P3HT:PCBM bulk heterojunction through morphological control without examining how the microstructure develops during the process. While a number of studies have attempted to resolve how the bulk heterojunction morphology develops during processing, many of these explanations contradict one another. For example, Schmidt-Hansberg *et al.*[80] and Kozub *et al.*[81] hold the view that the crystallisation of P3HT during annealing pushes the PCBM molecules out of the crystalline regions which causes fullerene aggregation and phase separation. The polymer-fullerene interactions overcome the fullerene-fullerene interactions such that the PCBM molecules only aggregate at a later stage after the molecular ordering of P3HT has started. Conversely, Beal *et al.*[82] believe that the de-mixing is induced by the aggregation of PCBM molecules during annealing in order to decrease the surface energy. The diffusion of fullerene out of the amorphous P3HT enables the polymer to crystallise without disruption.

Several questions can then be put forward: first, how does the morphology of a P3HT:PCBM bulk heterojunction develop along the timescale of processing, particularly during that of the most basic and most effective method, that is thermal annealing, and will it change with varying conditions? Second, how do P3HT crystallises in solution with time?

This study will attempt to establish a correlation between the processing parameters and the morphology of solution-processed P3HT:PCBM photovoltaics. The effects of thermal annealing, annealing temperature and PCBM concentration on the morphology of the P3HT:PCBM films will be examined through optical microscopy, atomic force microscopy (AFM), x-ray diffraction (XRD) and scanning electron microscopy (SEM). It is then followed by a benchmarking study of the kinetics of P3HT crystals nucleation and growth through the analysis of P3HT solutions using UV-Vis and films using AFM.

# Chapter 3

# Methodology

## 3.1 Sample preparation

P3HT (Rieke Metals, electronic grade, >96% regioregularity) and PCBM (Solenne, >99.5% purity) with mass ratios of 1:1, 1:0.67, 1:0.43, 1:0.25 and 1:0.11 were dissolved in chlorobenzene (Sigma-Aldrich, for HPLC, 99.9%) and stirred for 2 hours with a magnetic stirrer. The solid loadings were varied between 0.5 to 10 wt% in chlorobenzene to obtain films with different thicknesses. Next, the solutions were filtered with 0.45 µm PTFE syringe filters to remove any dust and potential aggregates. Although there is a risk that in filtering the solutions, we also removed the aggregates of only one component and not the other, thus changing the concentration of the blend, we have neglected this effect because the chlorobenzene is a good solvent for both the P3HT and PCBM, and that the solutions were visibly clear.

This paper uses the PCBM mass percentage with respect to the total mass of solids to name the samples. As such, the control of this study, which composed of only P3HT, is identified as 0% PCBM. Similarly, a sample with a P3HT to PCBM mass ratio of 9:1 is identified as 10% PCBM and so on.

In order to achieve the same film thickness for all films, a calibration curve of film thickness was produced across different ratios of P3HT to PCBM and solid loadings in chlorobenzene. A DektakXT Profilometer was used to determine the thickness of the films by cutting a groove with a needle and measuring the depth of the groove. The measurements were performed at a rate of 50 µm/s and with 2 mg force.

The data in Figure 3.1a were plotted from annealed films deposited through spin-coating at 1000 rpm for 60 seconds. The spin-coater allows films with homogeneous thickness over a large area (1–10 $cm^2$) to be fabricated with high reproducibility. During the spin-coating process, the angular velocity removes excess solution and evaporates the solvent, leaving a thin film on the substrate. As expected, the film thickness is influenced by both the concentration and the composition of the solution. It is also obvious that P3HT has a greater influence on the film thickness than PCBM in the final film, especially as the solids concentration increases. On the other hand, re-plotting the film thickness against the P3HT concentration instead of

the total solids (Figure 3.1b) collapses the plot into a single curve with increasing slope which is identical to the P3HT curve in Figure 3.1a.

According to the calibration curve, the solid loadings that produce 300-nm thick films, the thickness at which the P3HT:PCBM films absorb the most photons[71], were 3.5, 3.6, 3.7, 3.8, 4.6 and 5.4 wt% solid in solution for 0%, 10%, 20%, 30%, 40% and 50% PCBM respectively. As listed in Table 3.1, these interpolations were confirmed through the actual thickness measurement of films using a profilometer.

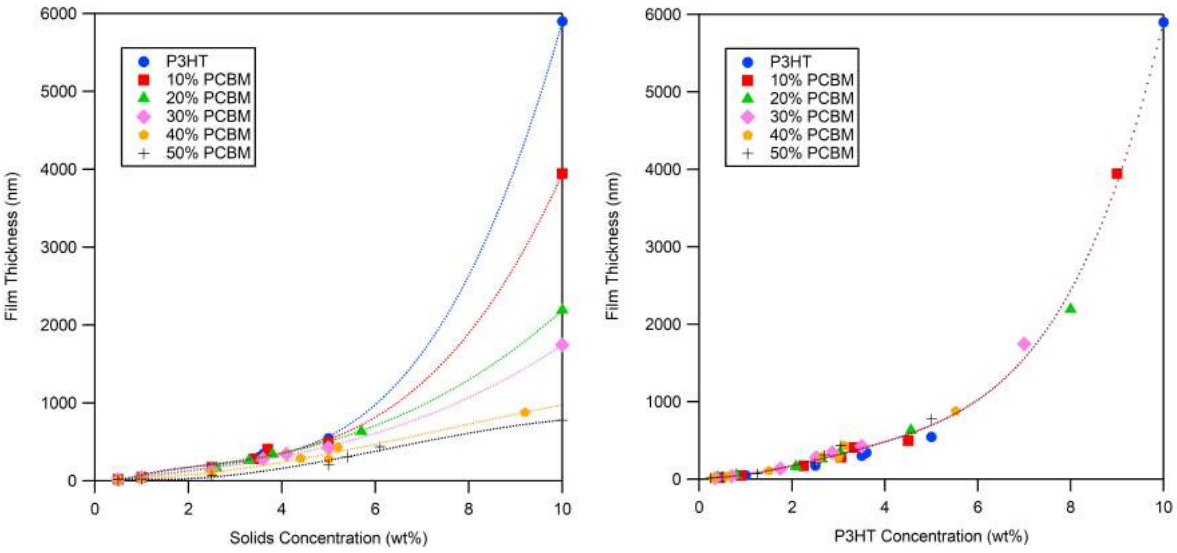


**Figure 3.1:** A plot of film thickness of various P3HT:PCBM ratios against (a) the total solid concentration and (b) the P3HT concentration. The dotted lines in the plots are fitted lines.

| PCBM loading (%) | Solid loading (wt%) | Film thickness (nm) |
|---|---|---|
| 0 | 3.5 | $298 \pm 7$ |
| 10 | 3.6 | $302 \pm 8$ |
| 20 | 3.7 | $300 \pm 8$ |
| 30 | 3.8 | $300 \pm 9$ |
| 40 | 4.6 | $300 \pm 7$ |
| 50 | 5.4 | $300 \pm 6$ |

**Table 3.1:** Measurement of film thickness with profilometer.

Directly after spin-coating, the films were thermally annealed inside a vacuum oven. As shown by the temperature profile inside the oven (Figure 3.2), the films were placed inside the oven initially at room temperature. After reaching the setpoint temperature, the oven was kept at 140°C for 1 hour before cooling down. Despite that, the oven only started to cool down roughly 3.5 minutes after the setpoint was reduced to room temperature. It is also important to note that it is very likely that the morphology of the films was already developing during heating up and still developing during cooling down because the temperature was above the glass transition temperature of P3HT:PCBM. Thus, in total, the films were annealed for more

than 1 hour.

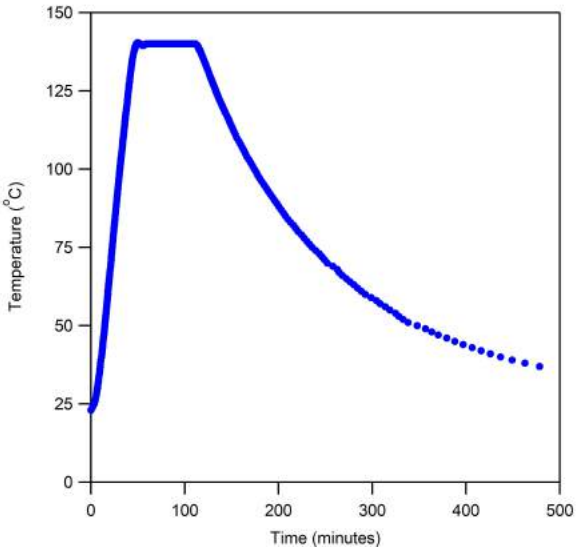


**Figure 3.2:** A plot of the temperature profile inside the vacuum oven during thermal annealing.

To induce nucleation and growth of P3HT fibres, P3HT was dissolved in p-xylene (Sigma-Aldrich, anhydrous, ≥99%) and heated to 80°C while stirring. After 30 minutes of heat treatment, the solution was slowly cooled down to room temperature and allowed to mature. It was during this ageing process that the P3HT fibres nucleated and grew.

As the substrate, silicon wafers were cut into 1 cm by 1 cm squares, followed by rinsing with distilled water (Millipore), drying with nitrogen gas (BOC, oxygen free) and UV ozone treatment for 1 hour. Subsequently, the solutions were pipetted onto the treated silicon wafers and spin-coated at 1000 rpm for 60 seconds under nitrogen atmosphere. The samples were then annealed in a vacuum oven at 140°C for 1 hour.

## 3.2 Optical microscopy

The optical microscopy was carried out with an Olympus BX60M microscope that was equipped a Nikon Digital Sight DS-Fi1 camera.

## 3.3 Atomic force microscopy (AFM)

The topography and phase images of the films were obtained using an Asylum Research Cypher ES. The scanning was performed at a frequency of 1 Hz in tapping (repulsive) mode using Tap300Al-G silicon AFM probes (resonant frequency: 300 kHz, force constant: 40 N/m) supplied by BudgetSensors. The images were subsequently modified using flatten 1 in the

MFP3D software.

## 3.4 X-ray diffraction (XRD)

The crystalline structure of the films was analysed with a Rigaku Ultima IV with an x-ray wavelength of 1.54 Å. While it was challenging to capture all the 'crystalline grains' within, the samples were rotated at 15 rpm during measurement to ensure that the equipment captured a statistical distribution of the crystalline grains.

## 3.5 Fourier-transform infrared spectroscopy (FTIR)

The IR absorbance spectra of the films were obtained using a PerkinElmer Spectrum 100.

## 3.6 UV-Vis

The growth of P3HT fibres in solution was analysed through obtaining periodic measurement of the solution's absorption spectrum using a PerkinElmer Lambda 35 UV/VIS Spectrometer.

## 3.7 Scanning electron microscopy (SEM)

In order to analyse the morphology of the films in the vertical direction, the films, along with the substrate, were cut in half and coated with platinum (Pt) in a Quorum Q150RS sputterer. Subsequently, the scanning electron images of the cross-sections were obtained using a Philips XL30S SEM with a voltage of 5 kV and spot size of 2.0.

## 3.8 Image analysis

The image analyses were carried out with an image processing software, ImageJ.

# Chapter 4

# Results and discussion

This project examined a series of model bulk heterojunction solar cells produced from a good solvent as well as thin film structures produced from a poor solvent. In the first experiment, P3HT and PCBM were co-dissolved in chlorobenzene, a good solvent for both the polymer and fullerene, and spin-coated to form films under ambient conditions. Whilst this particular system has been studied extensively, we chose to use ambient conditions towards a glovebox-free approach to scaling up the manufacture of plastic solar cells. In most instances, the thermal annealing conditions required to crystallise the P3HT simultaneously caused the PCBM to coarsen into microscale crystal aggregates, destroying the fine structure of the bulk heterojunction. To overcome this challenge, we pursued a method that enables the P3HT to crystallise in solution, potentially eliminating the need for thermal annealing.

The second section focusses on thin film structures of P3HT nanofibres grown from a poor solvent. In a poor solvent, P3HT tends to crystallise as long ribbons or fibres about 10 nm wide. Ageing a series of P3HT solutions created a distinct population of nanofibres, which grew and entangled, even forming gels at higher concentrations. The thin films produced from these solution exhibit percolated crystalline networks; the concentration and age of the solution control the thickness of the film and degree of percolation. Work is ongoing to determine whether these solution-grown nanofibres can be blended with PCBM to produce bulk heterojunctions that do not require annealing.

## 4.1 Nanostructural study of P3HT:PCBM film prepared from chlorobenzene

In this section, we provide a benchmark against previous results on the effects of thermal annealing, annealing temperature and composition on P3HT:PCBM films by varying the annealing temperature and P3HT:PCBM mass ratio, followed by investigating the optical microscopy images for any macroscopic phase separations, AFM images for the nanostructure and the diffraction patterns for the crystallinity of the films.

The optical microscopy images (Figure 4.1a–4.1f) revealed that the as-cast P3HT:PCBM films from chlorobenzene solution were smooth and homogeneous with no macroscopic structure visible. Parnell *et al.*[43] previously reported the presence of distinct phases within a P3HT:PCBM active layer. Any phase separation or microstructure, if present, must be smaller than a micron in size. Interestingly, the AFM topography images (Figure 4.2a–4.2e) also seem to indicate that there are some P3HT crystallites in the as-cast films in the form of short and thin fibres. Some P3HT crystallites were expected to form since the residual solvent in the as-cast film allows the P3HT chains to arrange themselves into a more energetically favourable structure[83]. Moreover, as with the case where P3HT chain ordering is induced in a marginal solvent[84], the concentrations of P3HT solution used in this study were above the solubility limit of P3HT in chlorobenzene, which is about 1.4 wt%[85]. This is supported by a study by Ameri *et al.*[86] where they were able to fabricate a completely amorphous P3HT:PCBM film (Figure 4.2g) without any crystallites from a 1 wt% solution. We, therefore, believe that some P3HT chains precipitate out of the solution into crystallites prior to casting. In the future, we will validate this using dynamic light scattering (DLS).

Furthermore, the AFM images seem to indicate that PCBM enhances the crystallisation of P3HT up to a 1:1 mass ratio, the maximum concentration of PCBM that was tested. As shown by Figure 4.2a–4.2e, the fibres formed in the films that contain PCBM were more defined than those in the neat P3HT film, and their thicknesses were found to increase in samples up to 40% PCBM. This suggests that PCBM serves as a nucleating agent for P3HT at low concentrations.

Additionally, the morphologies of the 40% and 50% PCBM samples appeared to be significantly smoother than the rest. As reported in previous studies[48,87], surface roughening is a characteristic of polymer crystallisation during annealing. Consequently, the reduction of surface roughness with increasing PCBM loading suggests that the PCBM molecules disrupt the crystallisation of P3HT in the as-cast films. This finding has been reported before by Tremolet de Villers *et al.*[88], where they observed that crystalline polymer domains were absent in films where nanoscale PCBM aggregates were present near the top surface. Therefore, it is possible that in the 10%–40% PCBM films, the PCBM molecules are dispersed, whereas in the 50% PCBM films, the PCBM molecules aggregate and disrupt P3HT crystallisation in the unannealed films.

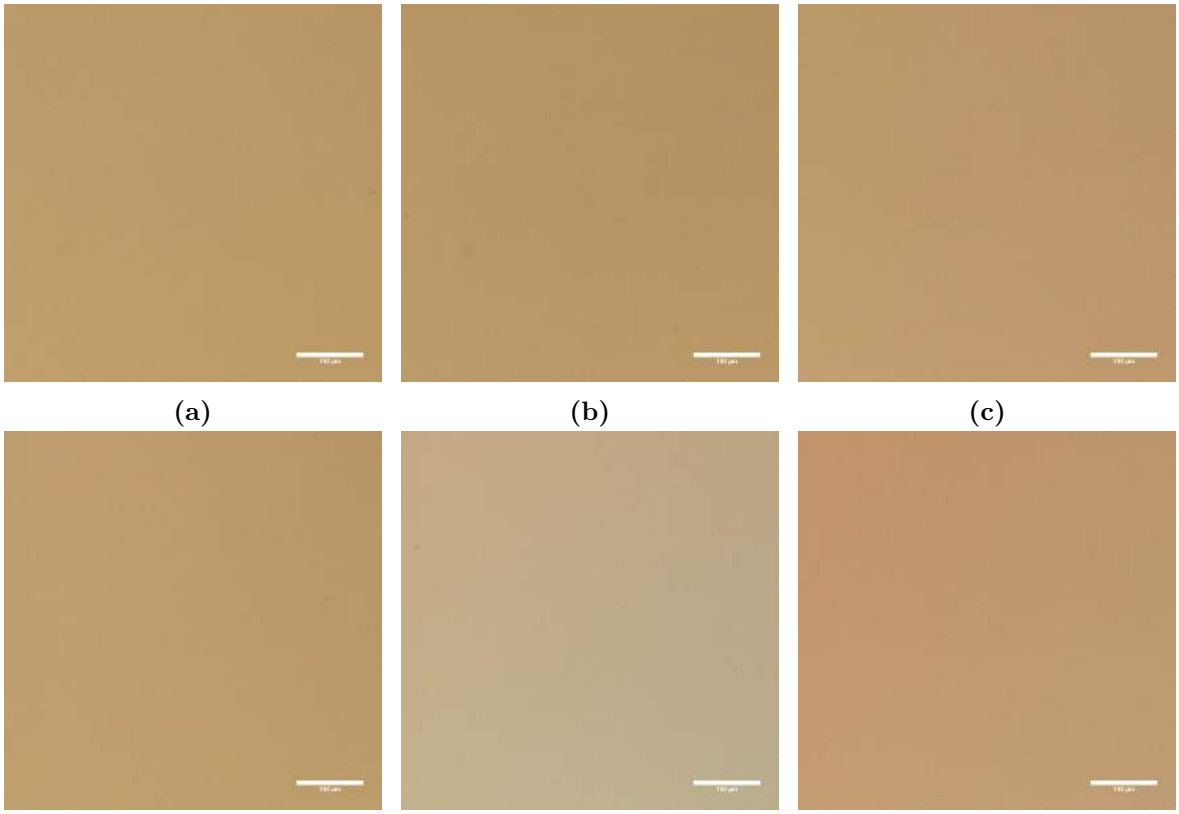

**(a)** **(b)** **(c)**

**(d)** **(e)** **(f)**

**Figure 4.1:** Optical microscope images of as-cast P3HT:PCBM films show homogeneous films with no macroscopic phase separation; (a) 0%, (b) 10%, (c) 20%, (d) 30%, (e) 40% and (f) 50% PCBM. The length of the scale bar is 100 µm.

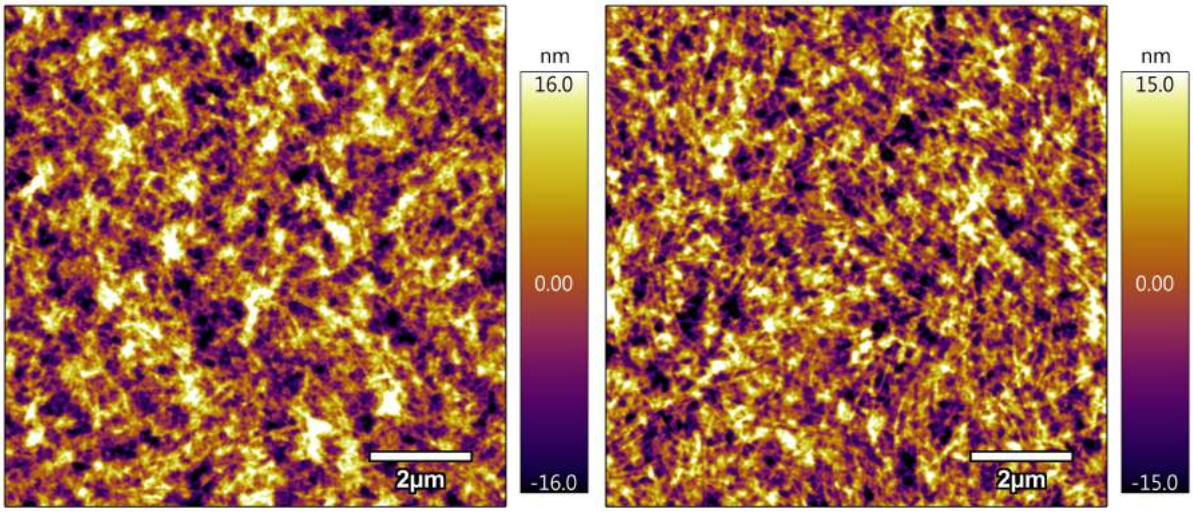
nm
16.0
0.00
-16.0
2µm

**(a)**


nm
15.0
0.00
-15.0
2µm

**(b)**

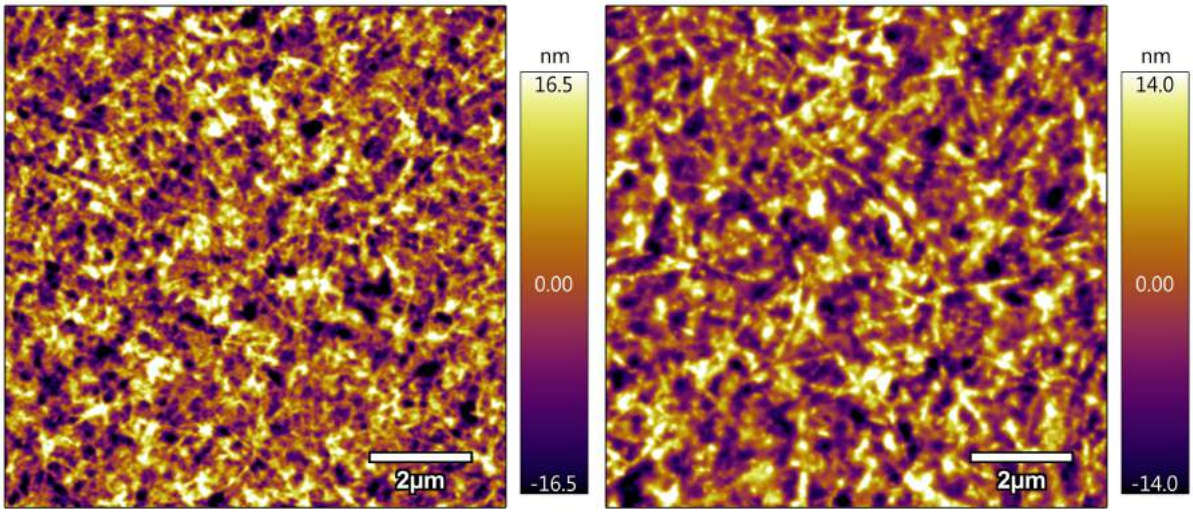
nm
16.5
0.00
-16.5
2µm
nm
14.0
0.00
-14.0
2µm

**(c)** **(d)**

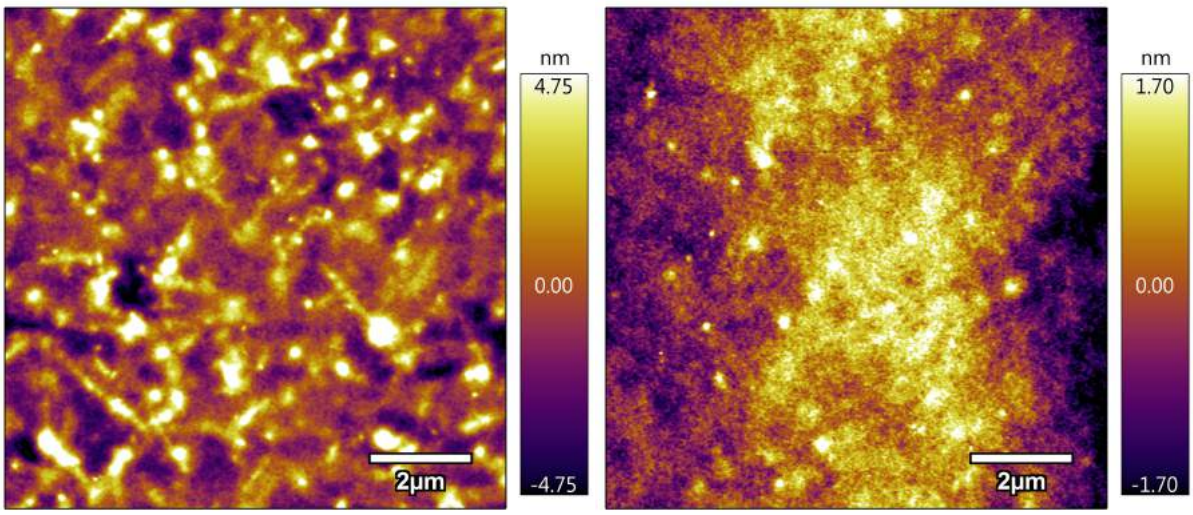
nm
4.75
0.00
-4.75
2µm
nm
1.70
0.00
-1.70
2µm

**(e)** **(f)**

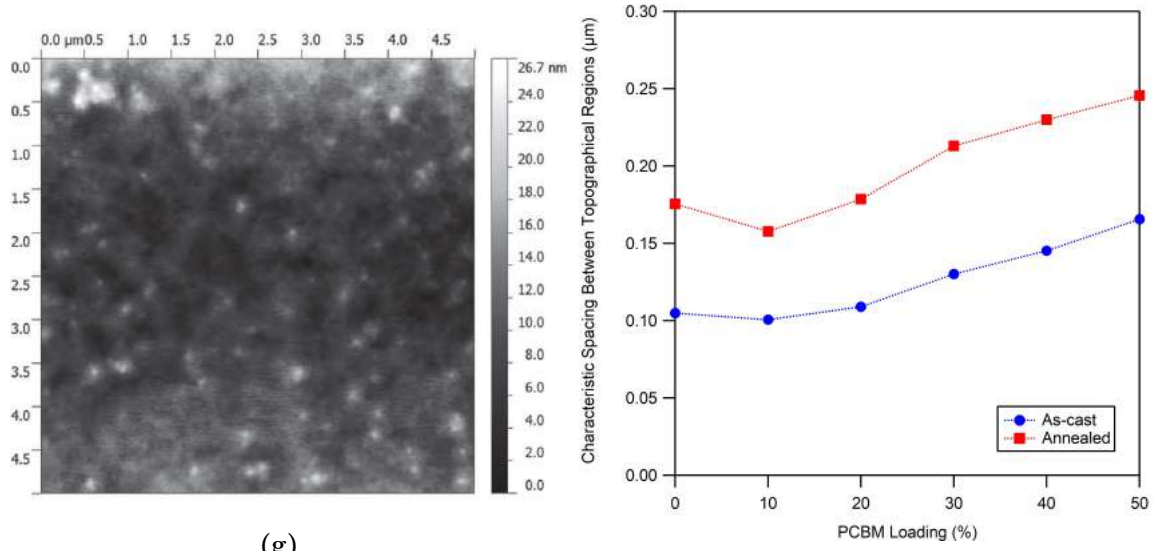


**(g)** **(h)**

**Figure 4.2:** AFM images of as-cast P3HT:PCBM films suggest the presence of polymer crystals in the films except at high PCBM loading; (a) 0%, (b) 10%, (c) 20%, (d) 30%, (e) 40% and (f) 50% PCBM; (g) an AFM image of amorphous P3HT:PCBM film that shows no fibres[86]; and (h) plot of the characteristic spacing between topographical regions obtained from FFT analyses against PCBM loading.

When the AFM images were subjected to Fast Fourier transform (FFT), they revealed a generally increasing characteristic spacing between topographical regions and that the 10% PCBM films exhibited the smallest spacing (Figure 4.2h). The FFT peaks, in this case, correspond to the size of the spacings between structures in the AFM images rather than the size of the crystals. This finding supports the observation from the AFM images, where, at low PCBM loading, the films are rough and randomly packed, and at high PCBM loading, the films are smooth and the structures are separated by an appreciable distance.

As confirmed by the XRD spectra of the as-cast films (Figure 4.3a), a small and rather broad (100) peak at $2\theta$ about 5.8° as well as weak (200) and (300) peaks correspond to a limited long-range order of P3HT which were assembled in the edge-on orientation, that is when the alkyl chains are aligned normal to the substrate[89], with a lattice spacing of 1.51 nm. The Scherrer equation states that the size of the crystalline domains in a solid is related to the broadening of a peak in a diffraction pattern. It is given as:

$$\tau = \frac{K\lambda}{\beta \cos\theta}$$

where $\tau$ is the mean size of the crystalline domains, $K$ is a dimensionless factor, $\lambda$ is the wavelength of the x-ray, $\beta$ is the full width at half maximum (FWHM) of a peak and $\theta$ is the Bragg angle. While it must be noted that the peak broadening in a diffraction pattern is also related to equipment smearing and that the Scherrer equation only applies to spherical crystals, this equation provides a means to indicate a trend in crystal sizes from diffraction patterns. From the edge-on peak, the average sizes of the crystalline domains in the as-cast films were estimated to be 117.1, 109.3, 107.3, 103.3, 81.3 and 64.1 Å for 0%, 10%, 20%, 30%, 40% and

50% PCBM respectively (Figure 4.3c; refer to Appendix A for the calculations). Furthermore, when the (100) peaks of as-cast films were normalised with respect to P3HT loading, they were found to be roughly the same, suggesting that there were similar proportion of edge-on crystals regardless of the composition (Figure 4.3d) and that there were, in fact, P3HT crystallites in the 50% PCBM films despite not appearing in the AFM image.

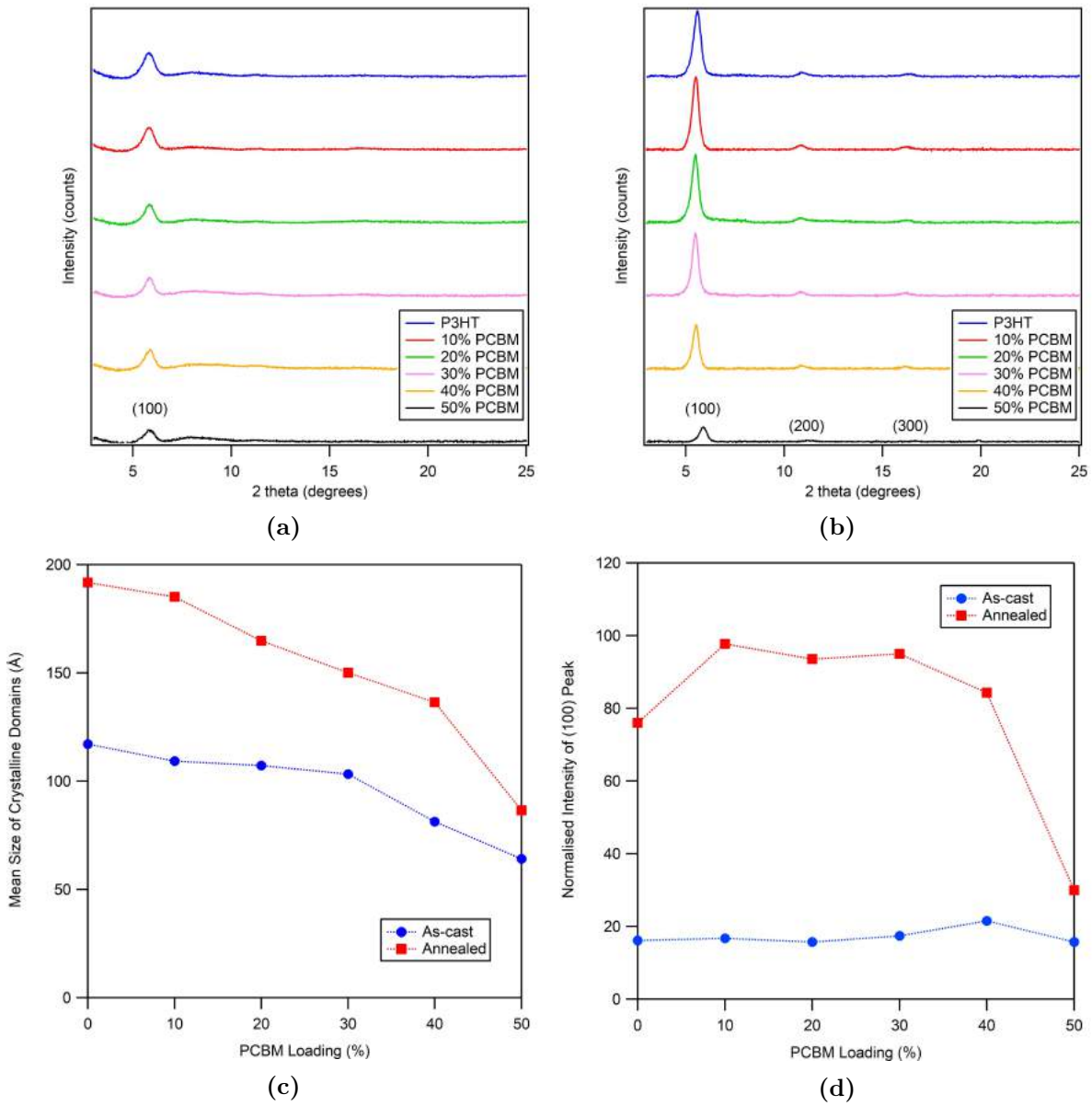


**Figure 4.3:** Diffraction patterns of (a) as-cast and (b) annealed P3HT:PCBM films; (c) plot of the mean size of crystalline domains of as-cast and annealed films, which was estimated using the Scherrer equation, against PCBM loading; and (d) plot of normalised intensity of (100) peak of as-cast and annealed films versus PCBM loading.

Our finding that the normalised (100) peaks were roughly the same for all as-cast films also suggests that PCBM has a negligible effect on the degree of crystallisation of as-cast films. It contradicts our previous observations from the AFM images which suggests that PCBM enhances P3HT crystallisation at low loadings and the opposite at high loadings. Further work

is needed to find an explanation for this discrepancy.

## 4.2 The effects of thermal annealing

Employing the same principle as the post-deposition annealing technique proposed by Padinger *et al.*[53], these films were subjected to heat treatment at 140°C under vacuum to prevent oxidation. As previously reported[62,90], the thermal annealing was found to induce phase separation. Here, micron-scale 'islands' were formed all over the films with PCBM content greater than 30% upon annealing as shown in Figure 4.4a–4.4f. These islands were assigned to PCBM aggregates as they were absent in the pure P3HT film and increased in number with PCBM loading. The thermal annealing, which was performed at a temperature above the glass temperature of P3HT, turned the P3HT matrix into liquid-like rubber and allowed the PCBM molecules to be mobile and diffuse through the amorphous P3HT matrix and aggregate, forming these micron-sized clusters. The average size of these aggregates was greater with increasing PCBM loading to a point between 40% to 50% PCBM, where the driving force for the nucleation of PCBM aggregates overcame that of growth (Figure 4.6a). Furthermore, each PCBM aggregate was surrounded by a 'ring' which was green in colour as a result of changes in film thickness (Figure 4.6b). Although previous study has attributed these 'rings' to the PCBM-depleted regions[91], where the PCBM molecules diffuse out to form large PCBM aggregates, it is likely that capillary forces play a larger role. We believe that these forces lead to the formation of meniscus around the PCBM aggregates that also depletes the polymer.

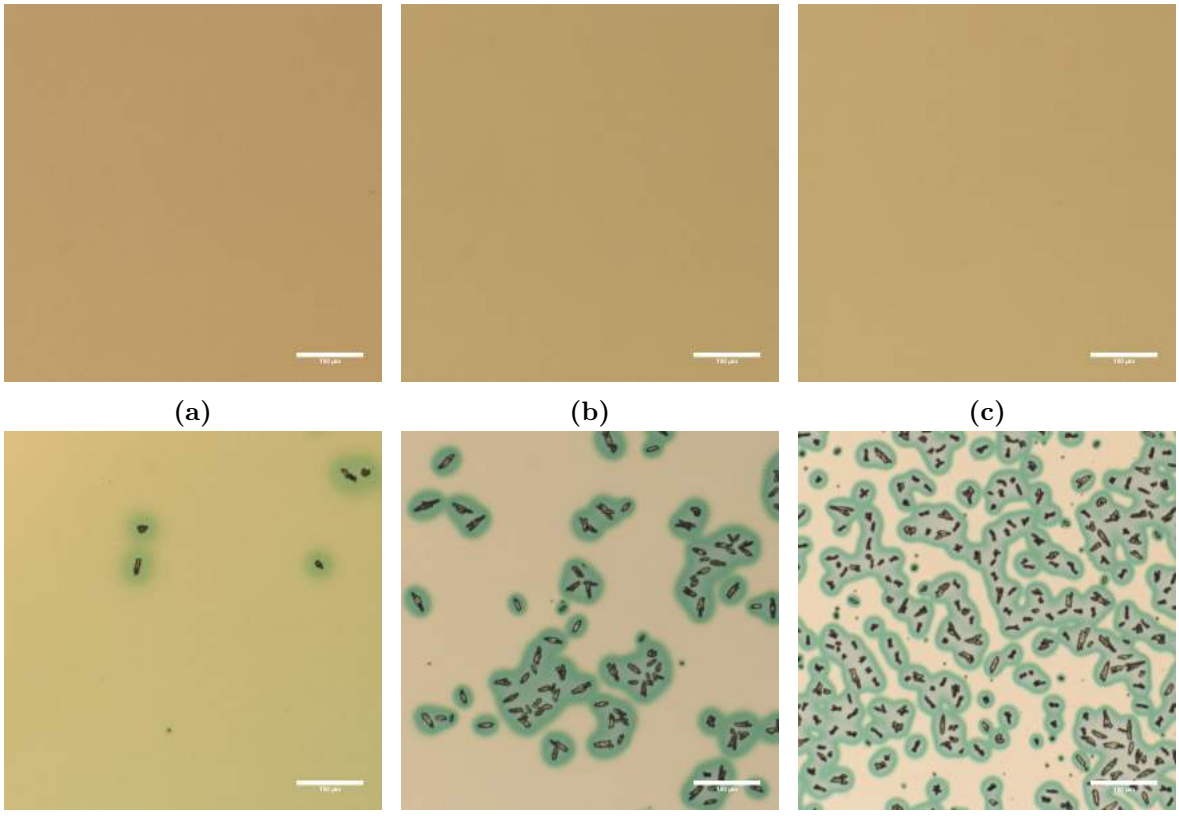


**Figure 4.4:** Optical microscope images of annealed P3HT:PCBM films demonstrate considerable phase separations at high PCBM loading and large PCBM aggregates surrounded by P3HT and PCBM-depleted regions; (a) 0%, (b) 10%, (c) 20%, (d) 30%, (e) 40% and (f) 50% PCBM. The length of the scale bar is 100 µm.

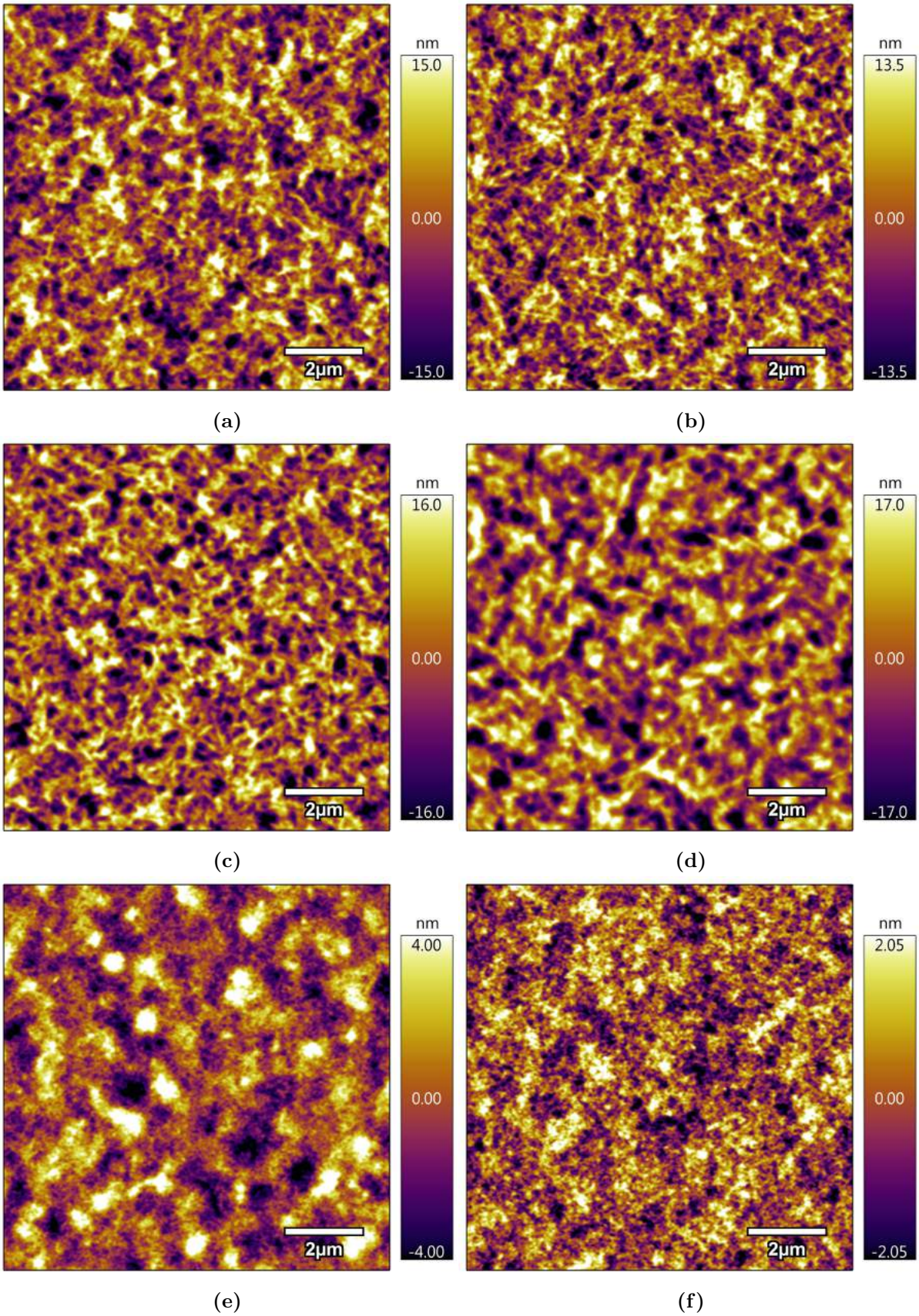


**Figure 4.5:** AFM images of annealed P3HT:PCBM films indicate the presence of fibrillar polymer crystals in the films except at high PCBM loading; (a) 0%, (b) 10%, (c) 20%, (d) 30%, (e) 40% and (f) 50% PCBM.

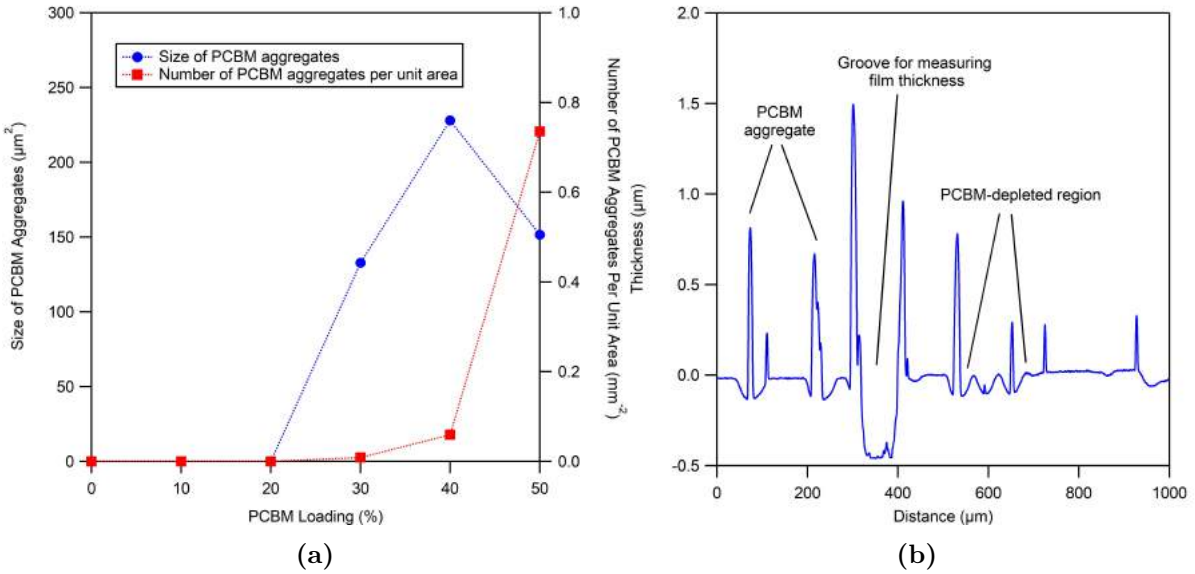


**Figure 4.6:** (a) plot of the mean size and the number of PCBM aggregates per unit area across different PCBM loading (they were absent in films below 30% PCBM); and (b) a surface profile of a 50% PCBM film shows PCBM aggregates (peaks) and depletion rings (wells).

As stated above, the PCBM aggregates were visible only on films with 30%, 40% and 50% PCBM loading. These observations agree with the findings by Watts *et al.*[65] as well as Kiel *et al.*[92], who confirmed that PCBM is partially miscible in P3HT and that more than two phases coexist in the annealed films. Although not shown here, it was observed that the PCBM started to form macroscopic aggregates when the P3HT:PCBM mass ratio was below 3:1, signifying the miscibility limit of PCBM in P3HT.

From the AFM images of the homogeneous regions of the annealed films (Figure4.5a–4.5f), it was found that thermal annealing increases the surface roughness of the films, while at the same time induces crystal growth, revealed as longer and denser fibres. These P3HT crystallites were surrounded by regions of intermixed P3HT and PCBM (Figure 4.7) to form a structure known as 'rivers and streams'[93]. This growth, however, was not observed in the AFM images of 40% and 50% PCBM films. Despite that, we will see later that the normalised diffraction pattern shows that 40% PCBM has roughly the same crystallinity as 0 to 30% PCBM films whilst 50% PCBM drops significantly in crystallinity.

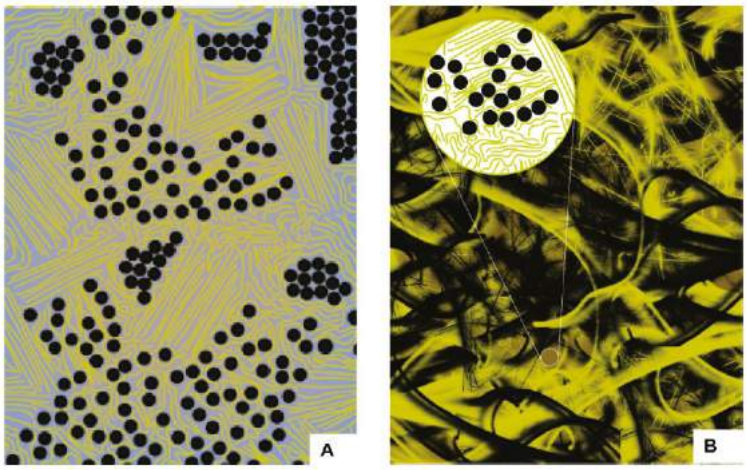


**Figure 4.7:** Rivers and streams model as proposed by Yin and Dadmun[93]. Annealed P3HT:PCBM films consist of at least three distinct phases: crystalline P3HT (yellow), crystalline PCBM (black) and a mixture phase.

Aside from the diffraction pattern of annealed 50% PCBM films, which was very similar to the as-cast films, the diffraction patterns of the annealed films displayed very distinct and sharp (100), (200) and (300) peaks that are typical of highly crystalline P3HT (Figure 4.3b). It demonstrates that the poorly ordered crystals that formed from spin-coating assume that of a lower energy upon annealing. The lattice spacing, that is the distance between two P3HT chains, was calculated to be 1.61 nm, signifying that the ordering of P3HT and PCBM is followed by an increase in lattice spacing, visualised by the (100) peak shift (Figure 4.8). Similar to the findings by Vanlaeke *et al.*[94], the peaks that represent face-on and end-on orientations were not detected, which suggest that the majority, if not all, of the P3HT crystallites were assembled in the edge-on direction. Using the same technique as with as-cast films, the mean size of the crystalline domains in the annealed films were estimated to be 191.7, 185.1, 164.8, 150.1, 136.4 and 86.6 Å for 0%, 10%, 20%, 30%, 40% and 50% PCBM respectively (Figure 4.3c; refer to Appendix A for the calculations). While these findings clearly demonstrate that thermal annealing improves the crystallinity of the films, there are three possible explanations to this decreasing crystallite domains size trend: 1) the PCBM disturbs the crystallisation of P3HT in the film, or 2) the PCBM serves as nucleating sites for P3HT in the film, or 3) the PCBM molecules intercalate into the P3HT chains, disrupting the existing P3HT crystallites and resulting in discontinuous crystallite domains. However, both Treat *et al.*[63], who adopted a model system of P3HT:PCBM bilayer, and Schmidt-Hansberg *et al.*[80], who studied the in-situ evolution of P3HT:PCBM films during drying, were able to prove that the diffusion of PCBM does not disturb the ordered stacking of existing P3HT chains and that the PCBM molecules are pushed out of the regions where the polymer crystallises and therefore, we rejected the last rationale.

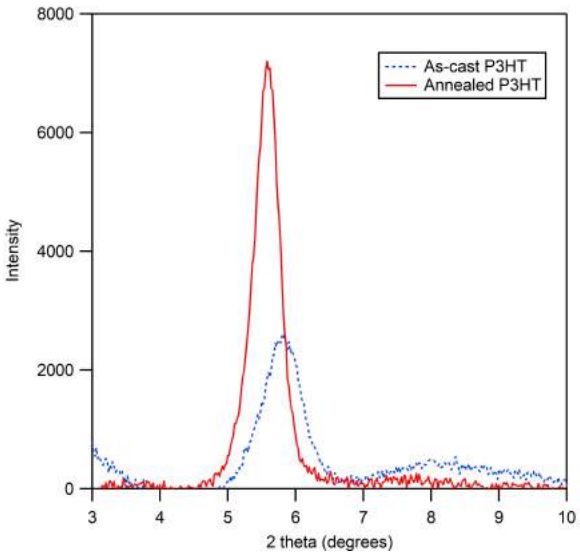


**Figure 4.8:** The diffraction patterns of as-cast P3HT (blue) and annealed P3HT (red) reveal a (100) peak shift upon thermal annealing.

Moreover, the plot of normalised intensity of the (100) peak (Figure 4.3d) showed that the intensity is maximum when the mass ratio of P3HT:PCBM is at 9:1. Although it decreased with increasing PCBM loading, at 40% PCBM, this intensity was still higher than pure P3HT. It suggests that the PCBM, below 1:1 mass ratio, does, in fact, induce P3HT crystallisation and that the effect was emphasised by the thermal annealing. Therefore, it is reasonable to hypothesise that PCBM provides nucleating sites for P3HT crystals to grow at low to moderate loading.

Similar to previous studies[61,89,95], no PCBM peaks were detected in the diffraction patterns of the annealed films. It was unlikely that the PCBM crystallites were absent due to insufficient annealing time because studies have shown that PCBM crystallites do form even after only 30 minutes of thermal annealing[96,97]. Although, as Erb *et al.*[89] attested, the absence of PCBM peaks might suggest that the PCBM aggregates were not crystalline, Berriman *et al.*[97] were able to prove otherwise. They discovered that the PCBM islands were, in fact, disordered aggregates of PCBM crystallites. We then hypothesised the reason behind the absence of PCBM peaks in the diffraction patterns of our annealed films to be the sample preparation method, where we measured the diffraction pattern of the films in contrast to their method of scraping and breaking the films into powders. As a result, the incoming photons do not sample a statistically relevant number of PCBM crystallites or that, since the samples were thin films, the intensity of the scattered photons might not be strong enough to be detected. It also explains why Erb *et al.*[89] only managed to obtain PCBM peaks from powder but not from thin films.

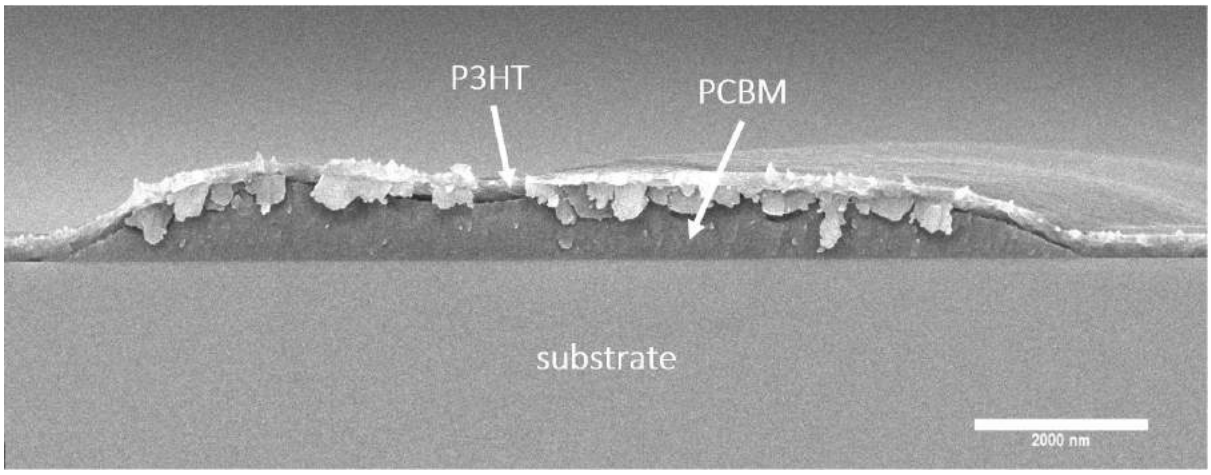


**(a)**

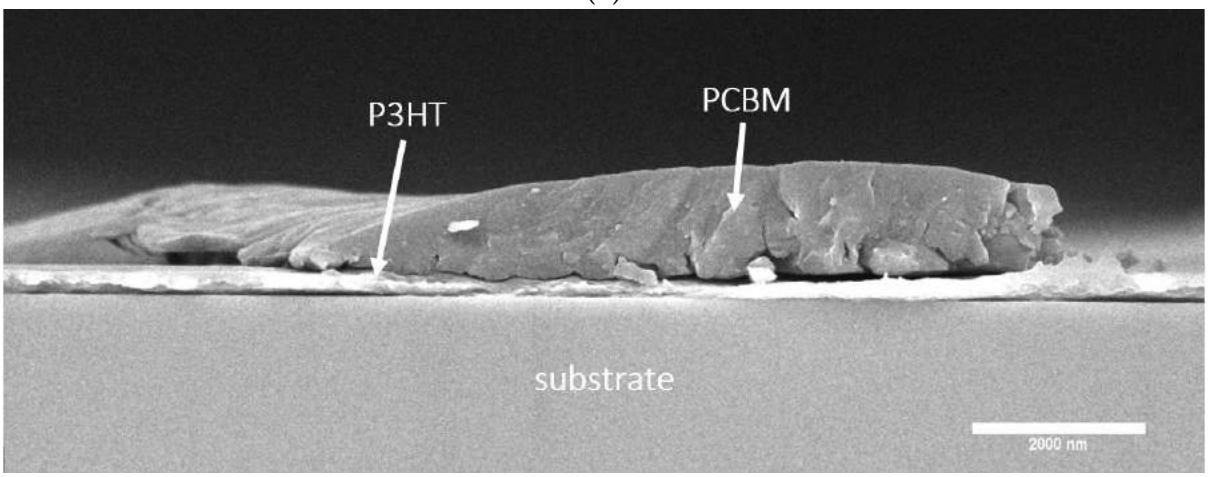


**(b)**

**Figure 4.9:** SEM images of the cross-section of annealed (a) 40% and (b) 50% PCBM films demonstrate two possible morphology development: (a) PCBM aggregates on the substrate and enveloped by a skin layer, and (b) PCBM aggregates on top of the film. The length of the scale bar is 2000 nm.

To investigate the morphology of the film in the vertical direction, the annealed films were mechanically ruptured at room temperature and analysed under the SEM. Initial observations revealed that the PCBM was brittle as shown by the clean-cut surface and the P3HT was more ductile (Figure 4.9a). The thickness of the PCBM aggregates was found to increase with the PCBM loading and was revealed to be between 0.8 to 1.3 µm. These observations are consistent with the findings by Berriman *et al.*[97] who discovered that the aggregates were considerably thicker than the film due to their low density. In the annealed 30% and 40% PCBM films, these massive aggregates were covered with a skin layer of P3HT (Figure 4.9a). Unfortunately, while the diffraction patterns of this films indicate that the P3HT crystals were edge-on, we were unable to confirm, whether the crystals in the skin region, if any, were also edge-on, or the equipment was not sensitive enough to detect a small population of another crystal orientation.

As was the case in this study, Watts *et al.*[65] and Xu *et al.*[98] also observed that the evolution of the bulk heterojunction morphology during thermal annealing was followed by a

vertical segregation of polymer and fullerene. They deduced that the driving force of vertical phase separation can be attributed to the difference in surface energy between atmosphere, P3HT, PCBM and the substrate. Since the surface energy of P3HT in air is lower than PCBM in air, the polymer tends to segregate to the top and the PCBM to the bottom, forming P3HT-air and PCBM-substrate interfaces. Despite that, this concept could not explain why the PCBM aggregates in the annealed 50% PCBM films rest above the film (Figure 4.9b), unlike in the 30% and 40% PCBM films. These observations provided evidence that the morphology evolution of the 50% PCBM films during thermal annealing proceeded through a different kinetic from the 30% and 40% PCBM films and that the overall morphology transformation of P3HT:PCBM films during annealing was driven by more than merely the difference in surface energy.

## 4.3 The effects of annealing temperature

We then continued by studying the effects of annealing temperature on the morphology of the films to gain a better understanding of the kinetics during thermal annealing. New as-cast films were thermally annealed at 100°C and 180°C. As shown in Figure 4.10a–4.10f, although the annealing temperature was above the glass transition temperature of the blend, the films which were annealed at 100°C did not form any PCBM aggregates. It suggests that the PCBM molecules did not have enough thermal energy to be able to move despite the polymer matrix being molten. Contrastingly, the films annealed at 180°C formed elongated PCBM aggregates which turned into 'fans' at higher PCBM loading (Figure 4.11a–4.11f), indicating that the PCBM aggregates grow anisotropically. Similar to the films which were annealed at 140°C, these aggregates were surrounded by PCBM-depleted regions but were larger in size. It was expected since more PCBM molecules were driven by the high thermal energy to diffuse through the polymer matrix to form larger aggregates. All in all, these observations demonstrated that the diffusion of PCBM in P3HT matrix is temperature-dependent.

Interestingly, however, the average size of the PCBM aggregates in the 50% PCBM films that were annealed at 180°C was found to be smaller than those of the 40% PCBM films. Despite having these large PCBM 'fans', the rod-like aggregates that did not form 'fans' were actually smaller than the aggregates in the 40% PCBM films. This behaviour is similar to the PCBM aggregates in films annealed at 140°C and, again, suggests that, at high PCBM loading, the nucleation of PCBM aggregates dominates over PCBM aggregates growth during the early stage of thermal annealing.

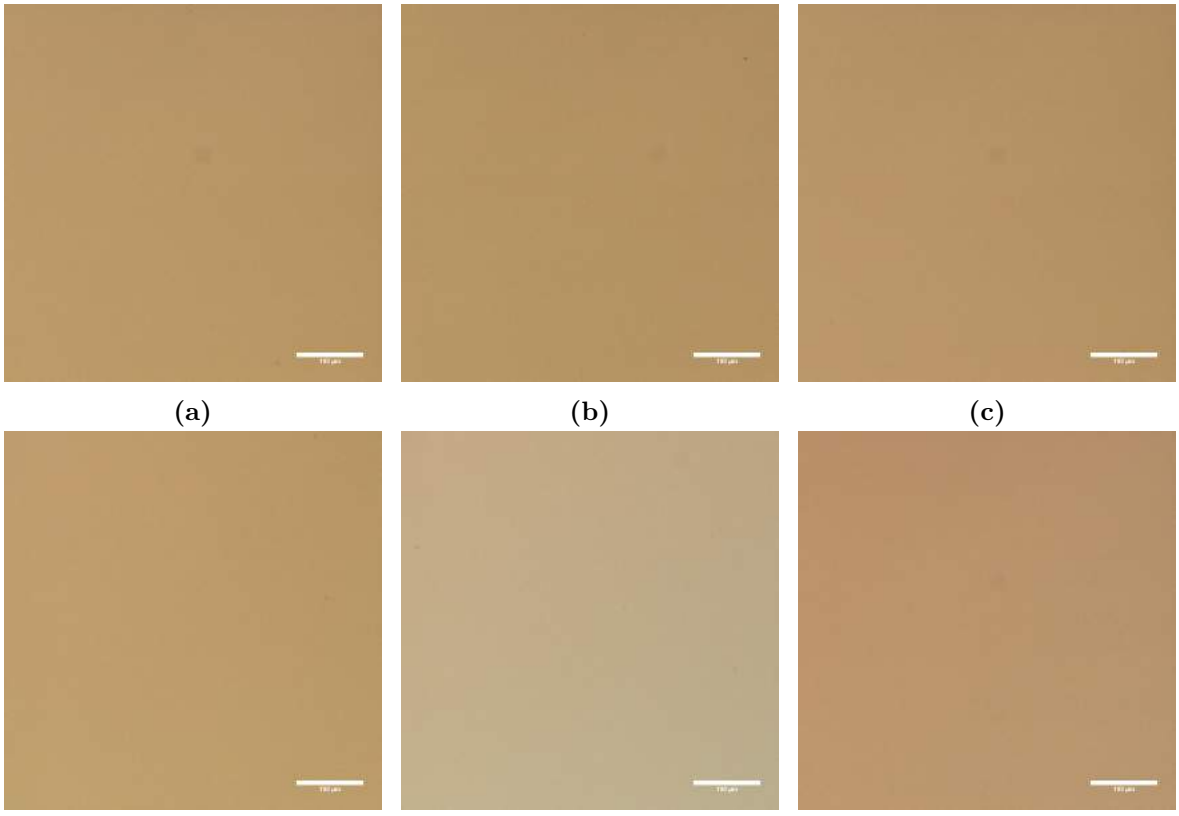

**(a)** **(b)** **(c)**

**(d)** **(e)** **(f)**

**Figure 4.10:** Optical microscope images of P3HT:PCBM films annealed at 100°C reveal homogeneous films with no macroscopic phase separation; (a) 0%, (b) 10%, (c) 20%, (d) 30%, (e) 40% and (f) 50% PCBM. The length of the scale bar is 100 µm.

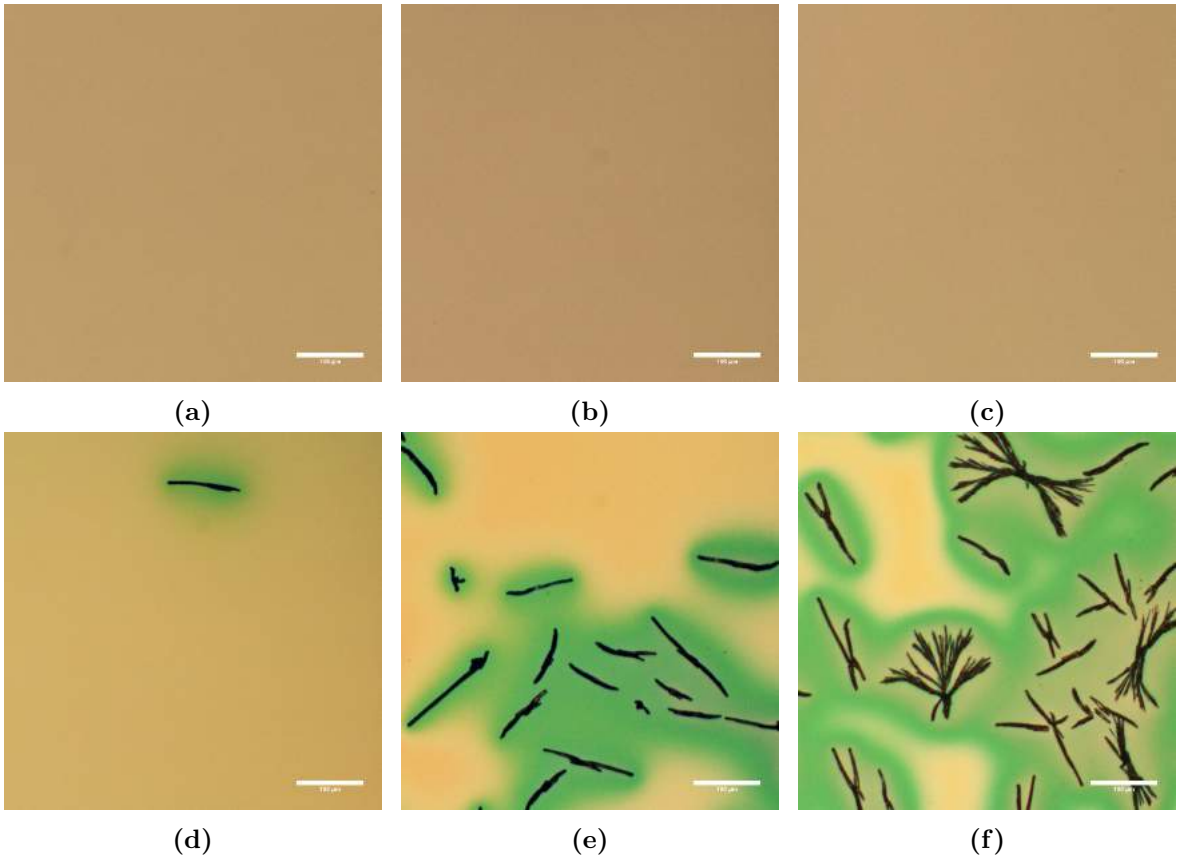


**Figure 4.11:** Optical microscope images of P3HT:PCBM films annealed at 180°C show extreme phase separation with elongated PCBM aggregates and 'fans' at high PCBM loading surrounded by P3HT and PCBM-depleted regions; (a) 0%, (b) 10%, (c) 20%, (d) 30%, (e) 40% and (f) 50% PCBM. The length of the scale bar is 100 µm.

Berriman *et al.*[97] proposed a model whereby the PCBM molecules precipitate to form aggregates in the as-cast films as the solvent evaporates and the pre-formed PCBM aggregates diffuse through the polymer matrix to aggregate during annealing. This model helps explain why the PCBM aggregates in the annealed 50% PCBM films, although greater in number, were smaller than those in annealed 40% PCBM films. Higher PCBM loadings give a larger number of initial PCBM crystallites in the as-cast film. As these crystallites diffuse through the polymer matrix, they aggregate and grow in size. Since there were plenty of PCBM molecules in the film, the PCBM aggregates grow rapidly. Due to their size, these large aggregates could only diffuse through the polymer matrix slowly and eventually serve as nucleation site for new PCBM aggregates. Moreover, a different study from the same group[99] successfully predicted using Flory-Huggins theory that the growth of PCBM aggregates ceases when the PCBM composition in the surrounding matrix reaches approximately 20% weight fraction. This value agrees with the miscibility limit of PCBM in P3HT as discussed before. Consequently, competing growth between pre-formed PCBM aggregates in the films annealed at 140°C lead to smaller final aggregates. Whereas in the case of the films annealed at 180°C, the PCBM precursors, possessing higher thermal energy, were able to diffuse through at a faster kinetics to aggregate with the neighbouring PCBM aggregates and eventually grow into 'fans'.

Therefore, the thermal annealing temperature plays an important role in determining the final morphology of the bulk heterojunction. At low temperature, there is insufficient thermal energy for PCBM to form micron-sized aggregates and as a result, phase separation is restricted. At medium temperature range, there is enough thermal energy for the PCBM to favour aggregate nucleation over growth. At elevated temperature, the thermal energy generates a balance between the PCBM aggregates nucleation and growth, resulting in significant phase separation. It is absolutely possible that at an even higher temperature, the kinetics shift to purely growth, producing a single large PCBM aggregate surrounded by a matrix of about 80% weight fraction P3HT and 20% weight fraction PCBM.

## 4.4 Solution-grown P3HT fibres

Although thermally annealing the P3HT:PCBM films increases the crystallinity of the polymer, it causes unwanted macroscopic aggregation of the fullerene. Several techniques have been proposed, such as using a co-solvent[47,48] and a nucleating agent[49] to induce P3HT crystallisation without annealing. However, these techniques introduce additional material into the system, resulting in increased complexity. Instead, we explored a technique of inducing P3HT ordering through heat treatment of the polymer solution. The advantage of this method is that it requires less processing. This method, as we will later see, also enables fine tuning of P3HT fibres morphology by changing the concentration and the ageing time. Furthermore, we chose just P3HT as a step towards blends and because the fibril formation in ambient has never been studied before. P3HT fibres were examined by varying the concentration of P3HT in the solution and then studying the absorption spectrum with time for fibres growth, AFM images for the nanostructure and FTIR for the crystallinity of the films.

In this study, P3HT fibres were fabricated using the same technique as Berson *et al.*[51] as well as McFarland *et al.*[52]. As was expected from a poor solvent, P3HT hardly dissolved in p-xylene at room temperature. Heating the solutions at 80°C for 30 minutes resulted in complete dissolution of P3HT and turned the colour of the solutions into bright and transparent orange (Figure 4.12). As suggested by Oosterbaan *et al.*[84], the formation of P3HT fibres was accompanied by a change in the colour of the solution from orange to purple. Here, the solutions maintained their colour when they were slowly cooled down to room temperature with a cooling profile as shown by Figure 4.13a and only started to gradually change their colour to dark purple after two hours at room temperature.

**Figure 4.12:** When P3HT is completely dissolved in p-xylene, the solution gives a bright orange colour (left). However, the colour of the solution changes with ageing to dark purple (right).

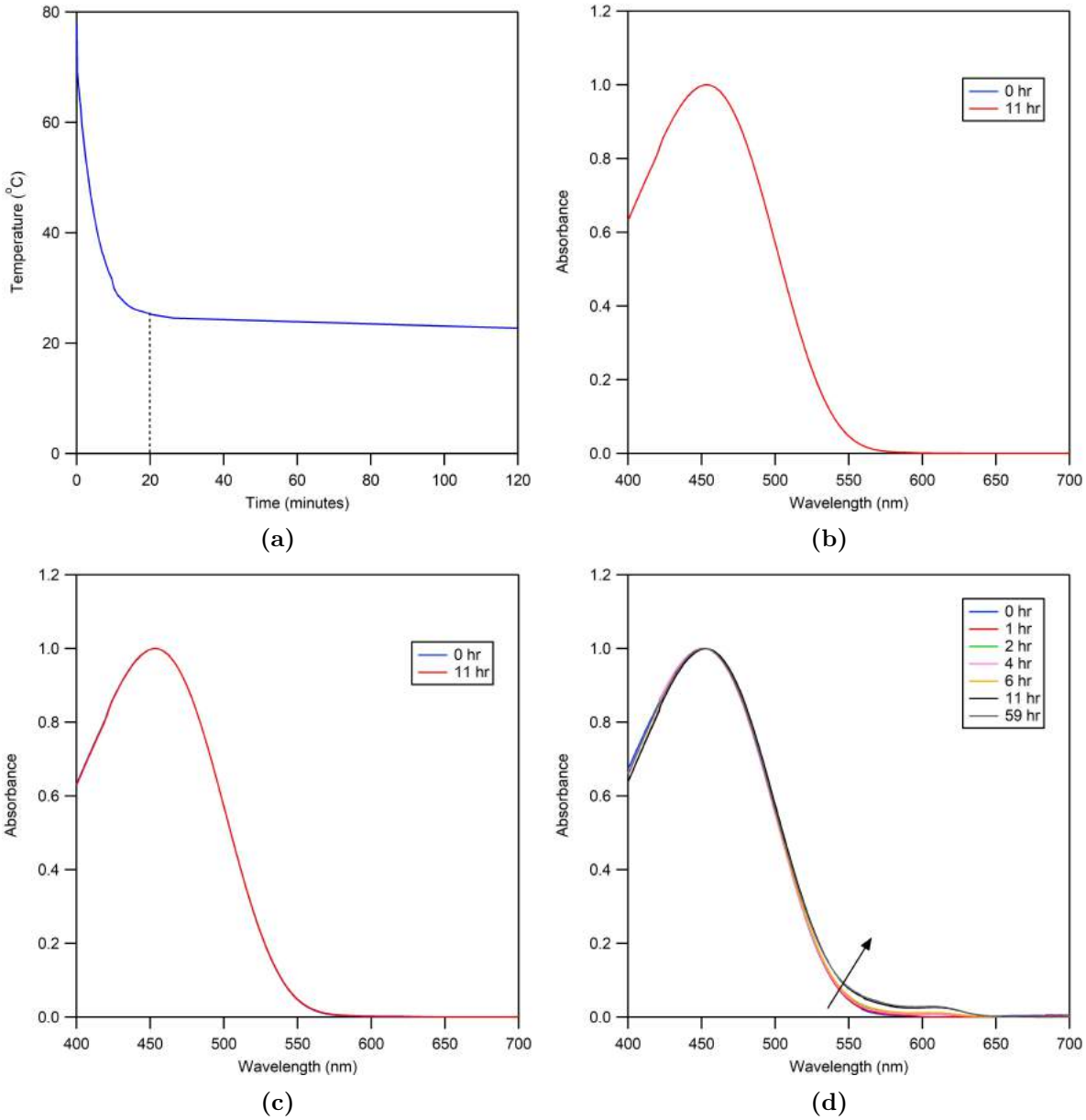

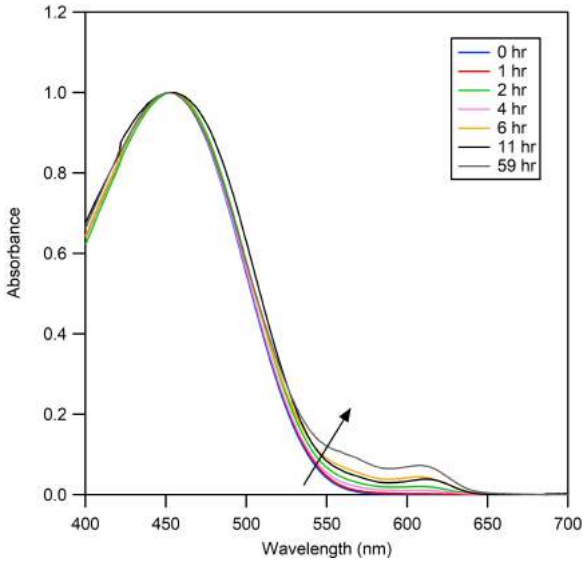
Absorbance
Wavelength (nm)
0 hr
1 hr
2 hr
4 hr
6 hr
11 hr
59 hr

**(e)**

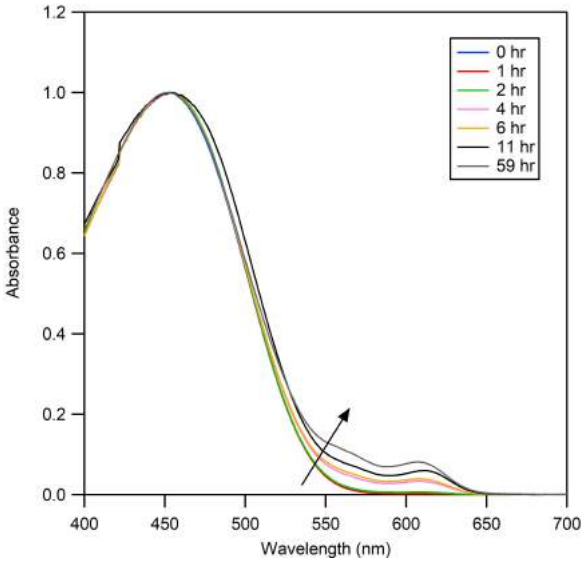
Absorbance
Wavelength (nm)
0 hr
1 hr
2 hr
4 hr
6 hr
11 hr
59 hr

**(f)**

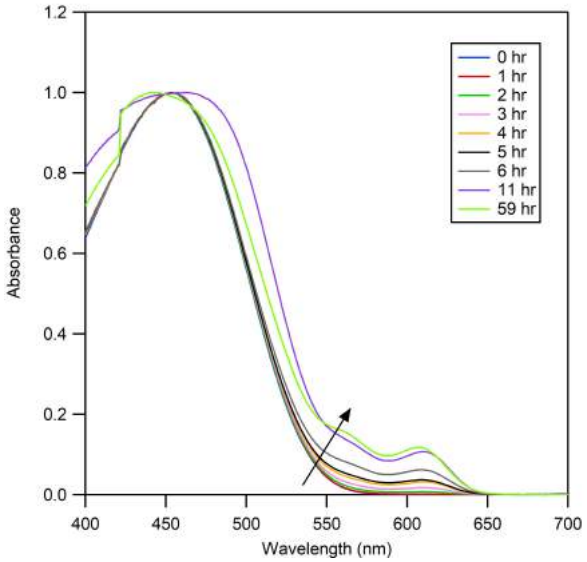
Absorbance
Wavelength (nm)
0 hr
1 hr
2 hr
3 hr
4 hr
5 hr
6 hr
11 hr
59 hr

**(g)**

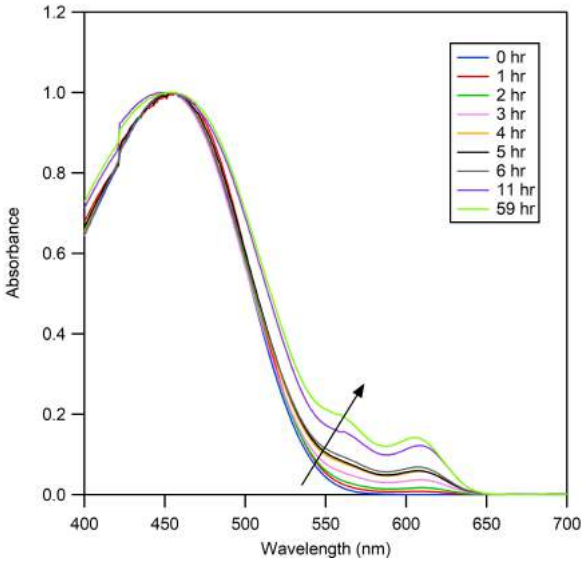
Absorbance
Wavelength (nm)
0 hr
1 hr
2 hr
3 hr
4 hr
5 hr
6 hr
11 hr
59 hr

**(h)**

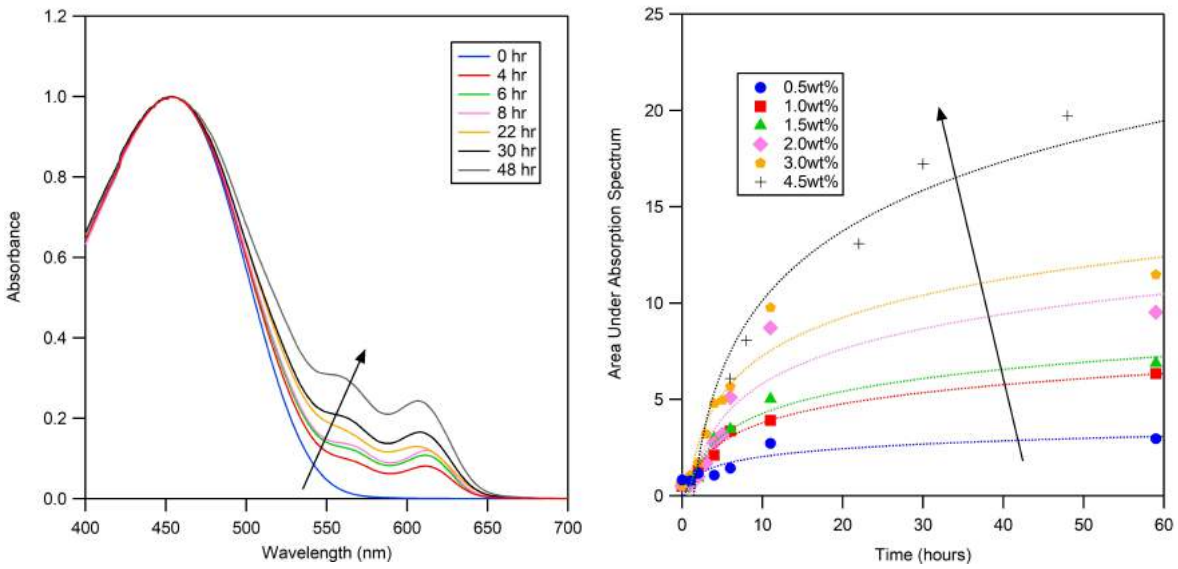


**Figure 4.13:** (a) temperature profile of the solution during cooling; the absorption spectra of (b) 0.1, (c) 0.3, (d) 0.5, (e) 1.0, (f) 1.5, (g) 2.0, (h) 3.0 and (i) 4.5 wt% P3HT in p-xylene indicate structural evolution with time (arrow lines indicate increasing time), except at very low concentration. The area under the two absorption peaks at 565 and 615 nm was plotted against time in (j), revealing a logarithmic growth. The dotted lines and the arrow line in (j) show Avrami equation fits and increasing solution concentration respectively.

The nucleation and growth of P3HT fibres over time were tracked using UV-vis. Figure 4.13b–4.13i showed the absorption spectra of 0.1, 0.3, 0.5, 1.0, 1.5, 2.0, 3.0 and 4.5 wt% P3HT in p-xylene. The first two concentrations showed a single amorphous peak without any change in the absorption spectrum after 59 hours of ageing. There was also no change observed in the absorption spectra of 0.5, 1.0 and 1.5 wt% solutions during the first 2 hours, suggesting that the polymer was still well dissolved and that nucleation was initiating slowly at room temperature. After 4 hours, two absorption peaks at 565 and 615 nm, which could be attributed to the 0–0 and 0–1 transitions of P3HT ordering through $\pi$-$\pi$ stacking[100,101], emerged. The onset of emergence of these two peaks, however, is dependent on the concentration of the solutions, with peaks appearing after only 2 hours for the 2.0 wt% solution and 1 hour for the 3.0 and 4.5 wt% solutions. The intensity of these absorption peaks slowly increased until approximately 48 hours after the end of the solution heat treatment. It was evident that both the rate and the extent of the P3HT fibres formation in the solution is influenced by the concentration of the solution. As shown by Figure 4.13j, the area under these peaks, which was obtained by subtracting the area under the curve of a solution of interest with that of a completely dissolved solution, were discovered to grow logarithmically over time and obey the Johnson-Mehl-Avrami-Kolmogorov equation, also known as the Avrami equation. The Avrami equation describes the transformation of a solid to a different phase at a constant temperature and is given as:

$$\Phi = 1 - e^{-Kt^n}$$

which can also be written as:

$$\ln \ln \frac{1}{1-\Phi} = \ln K + n \ln t$$

where $\Phi$ is the fraction of the P3HT crystal fibres, $K$ is a fitting parameter and is proportional to the volume of the sample and the nucleation rate, $t$ is time and $n$ is related to the dimension of the crystals formed[102]. In addition, according to the Beer-Lambert law, the absorbance of a solution is directly proportional to the concentration of the absorbing species. To make the calculations more straightforward, it was assumed that the concentration of the absorbing species is equal to the volume fraction of the P3HT fibres in the solution. As a result, the dimension of the P3HT crystals could be approximated using the plot of absorption against log(time) (Figure 4.14). The P3HT crystals formed in p-xylene were estimated to be one-dimensional in 0.5, 1.0 and 1.5 wt%, two-dimensional in 2.0 and 3.0 wt% and four-dimensional in 4.5 wt% solutions. The latter was not surprising given the fact that the 4.5wt% solution turned into gel when matured, suggesting that at high concentration, the P3HT fibres were sufficiently long that there were significant inter-fibre interactions. These findings indicated that the kinetics and the resulting structure of the fibres that formed in the solution are strongly influenced by the concentration of the species.

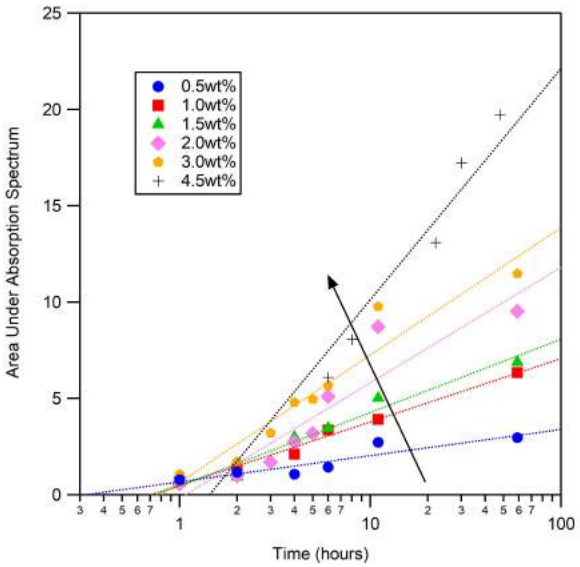


**Figure 4.14:** A plot of area under the absorption spectrum against log(time) shows straight Avrami equation fits (dotted lines). The dimensions of the fibres were determined from the slope of the fits. The arrow line represents increasing P3HT concentration.

Subsequently, thin films were fabricated from solutions across different ageing times. We were, however, unable to fabricate a homogeneous thin film from the 4.5 wt% solution due to gelation. The films that were spin-coated from heated 0.1, 0.3, 0.5 and 1.0 wt% solutions were smooth and homogeneous without any particular structure (Figure 4.16a, 4.17a, 4.18a and 4.19a), suggesting that the P3HT chains were amorphous. Remarkably, all solutions displayed some P3HT fibres at various ageing times despite the absorption spectrum showing no crystalline P3HT peaks. The fibres started to appear after 4 hours for 0.1 wt% (Figure 4.16b) and 2 hours for 0.3, 0.5 and 1.0 wt% (Figure 4.17b, 4.18c and 4.19c). They signify that the crystal nucleation in the solution, as a matter of fact, began at an earlier stage after heat treatment, indicating that UV-Vis, as a technique to track crystal growth, is less sensitive to

crystal formation than microstructure analysis with AFM. Furthermore, at even higher P3HT concentrations, such as the 1.5, 2.0 and 3.0 wt% solutions, the fibres were present immediately after heat treatment (Figure 4.20a, 4.21a and 4.22a). Future work will pursue DLS as a more sensitive technique for assaying the presence of nanofibre crystals. As a proof of concept, Figure 4.15 visualises the DLS data obtained from a P3HT solution while it was heated and after maturation. It shows that ageing the solution gives rise to an increase in particle size.

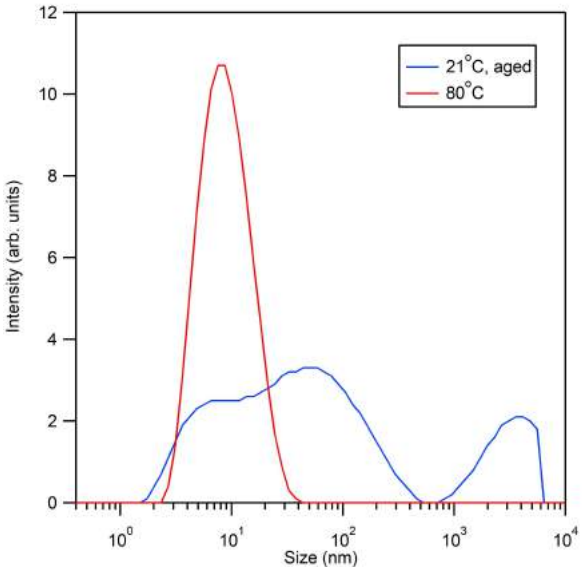


**Figure 4.15:** A plot of DLS data of P3HT in p-xylene during heating (red) and after ageing (blue).

As revealed by the AFM images, the number density and the length of the fibres increase with time and were accompanied with an increase in surface roughness. At 96 hours, most of the films consisted of mostly entangling fibres and minimal amorphous fraction with the exception of the 0.1 wt% films. These images serve as a clear evidence that the rate of P3HT crystallisation is concentration-dependent and that it is possible to fine-tune the fibres morphology by changing the concentration of the solution. Furthermore, as demonstrated by the 0.1 and 0.3 wt% films, it also shows that the formation and growth of P3HT fibres occurred even below the reported solubility limit of P3HT in p-xylene, which is 0.39 wt%[103].

Although the absorption peaks did not change after about 96 hours, it was almost impossible to validate whether extended ageing resulted in further fibre nucleation and growth as it was difficult to detect from the AFM image. It is, however, important to state that even after 96 hours of ageing, not all of the P3HT crystallised into fibres. Previous studies have deduced that only about 30-60% of the total P3HT in solution can form crystals due to thermodynamic limitations, such as the entropy of the system[104,105]. However, we doubt it since the thermodynamic driver for crystallization is very strong and the lattice enthalpy of crystal formation significantly lowers the free energy of the system. In contrast, we believe that the reason P3HT never reaches full crystallinity is because the dynamics of chain motion limit the complex folding structure that would be required. As the sample crystallizes, it is increasingly hard for the amorphous segments to diffuse over to the crystalline segments, and as

a result the structure gets 'stuck.' Unfortunately, we were unable to quantify the crystallinity in a thin film due to the limitations of the available equipment.

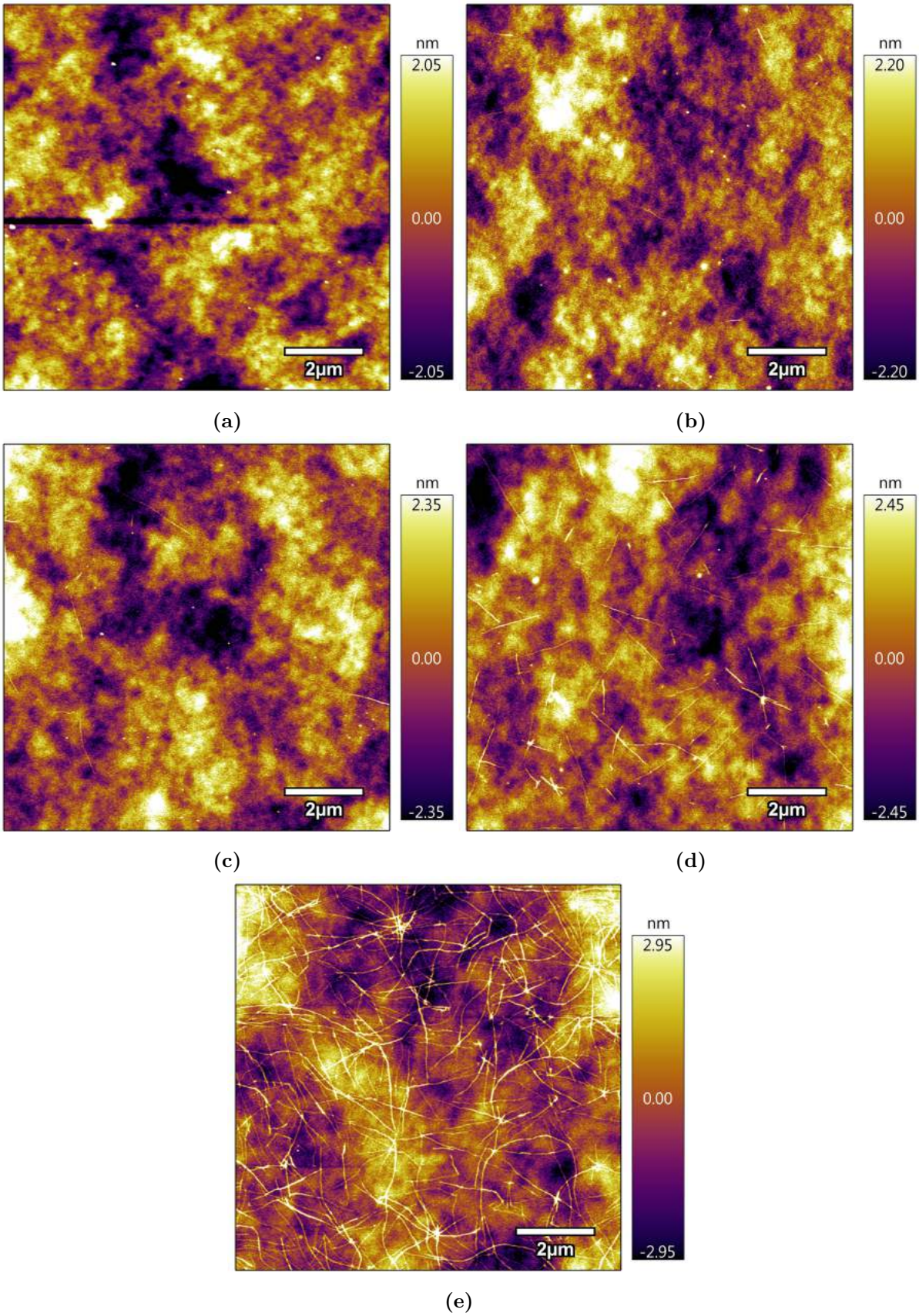


**Figure 4.16:** AFM images of as-cast films that were fabricated from 0.1wt% P3HT solution at (a) 0, (b) 4, (c) 12, (d) 24, (e) 96 hours.

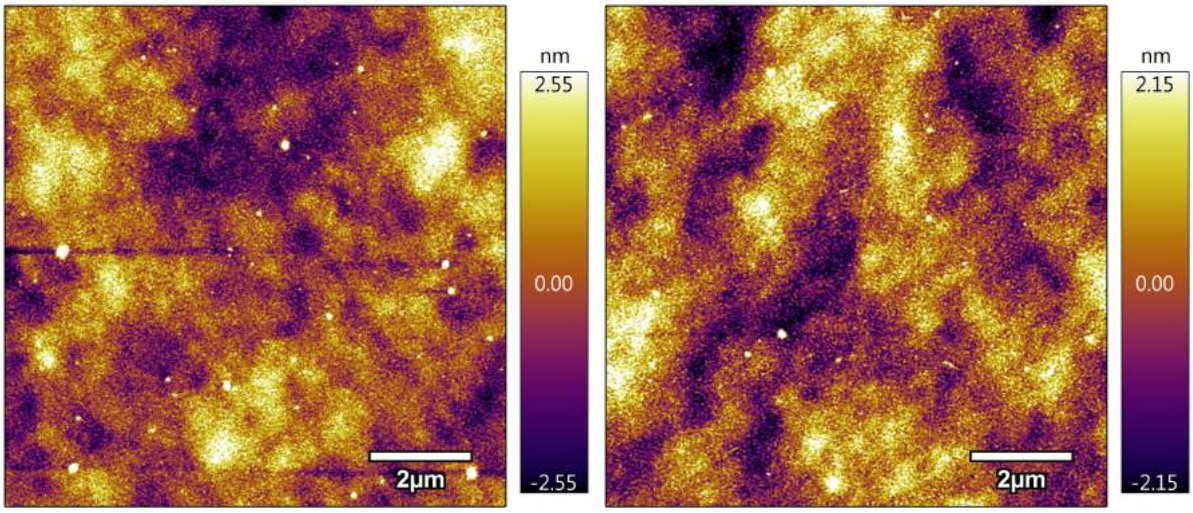
nm
2.55
0.00
-2.55
2μm

**(a)**


nm
2.15
0.00
-2.15
2μm

**(b)**

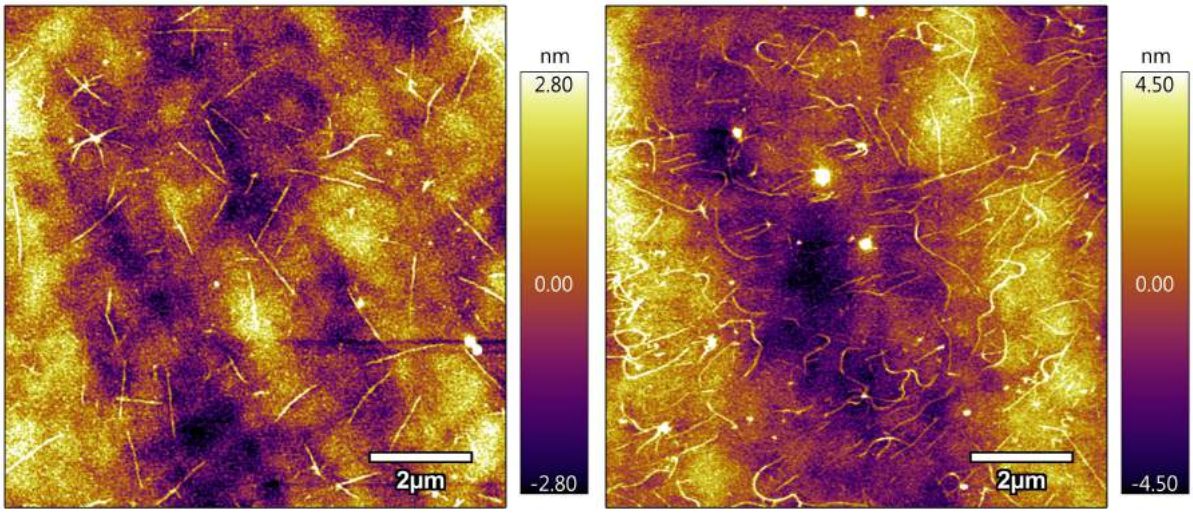
nm
2.80
0.00
-2.80
2μm
nm
4.50
0.00
-4.50
2μm

**(c)** **(d)**

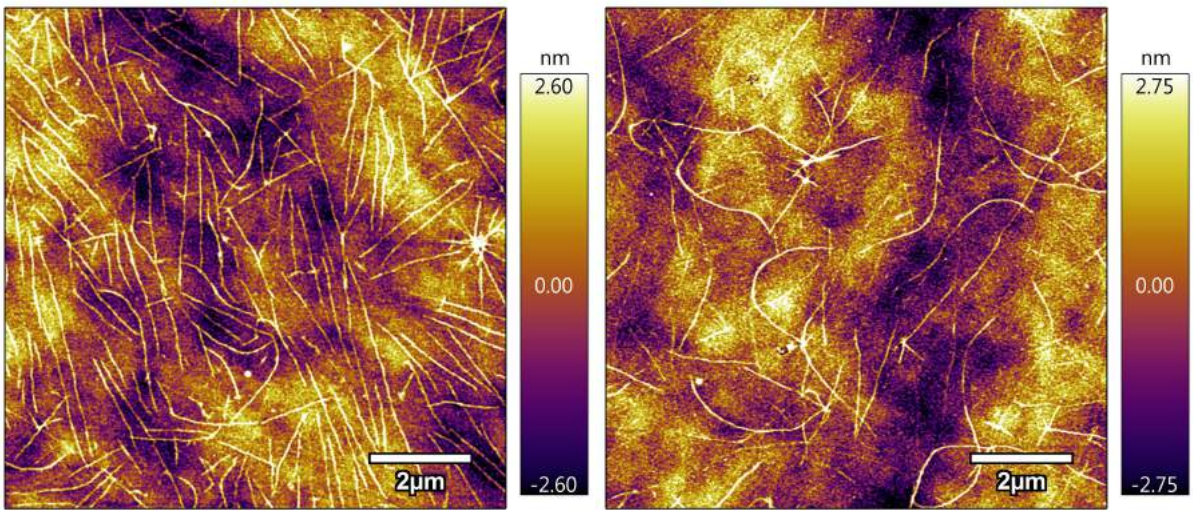
nm
2.60
0.00
-2.60
2μm
nm
2.75
0.00
-2.75
2μm

**(e)** **(f)**

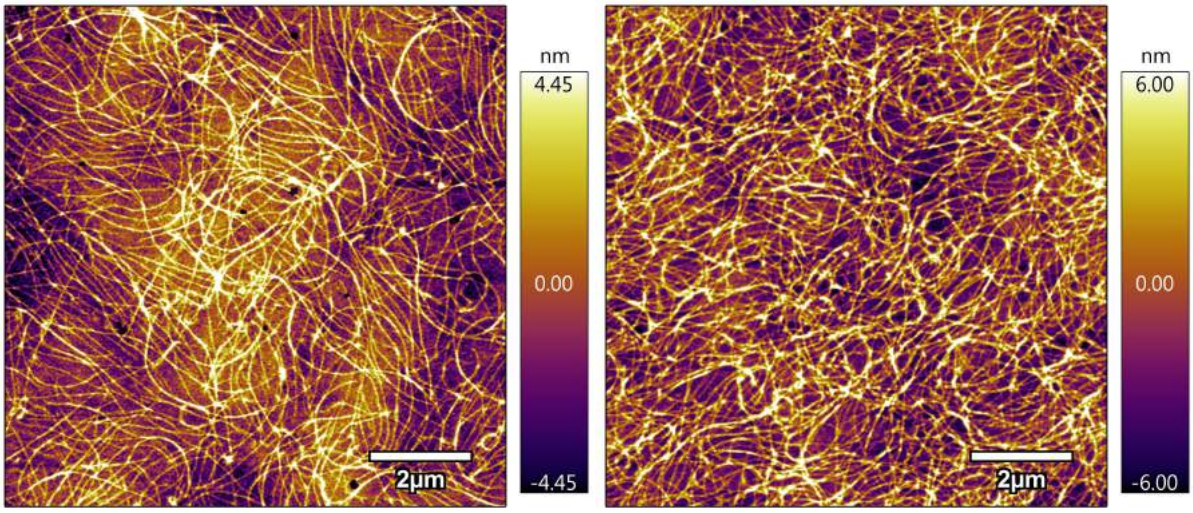


**(g)** **(h)**

**Figure 4.17:** AFM images of as-cast films that were fabricated from 0.3wt% P3HT solution at (a) 0, (b) 2, (c) 3, (d) 4, (e) 6, (f) 12, (g) 24 and (h) 96 hours.

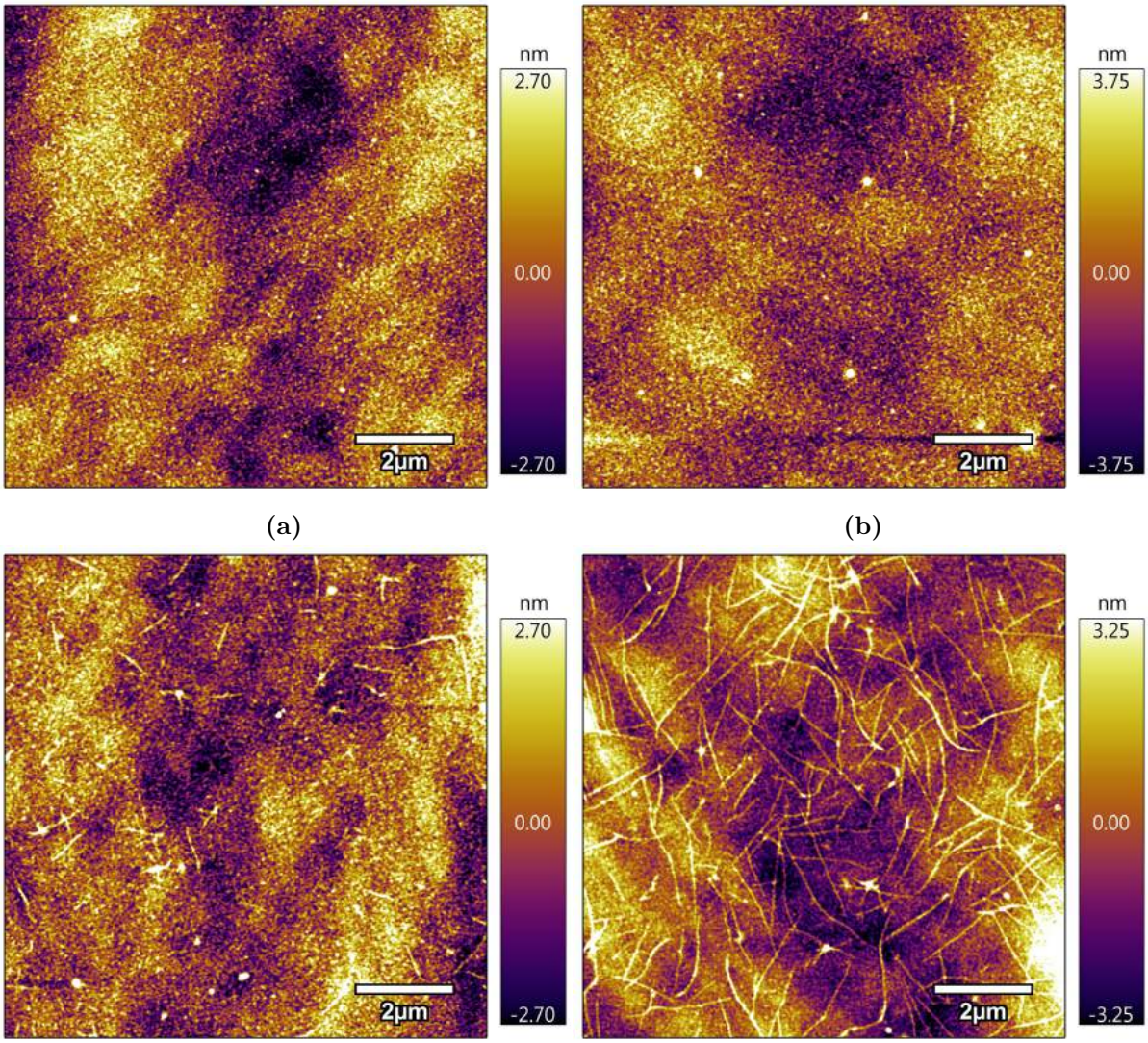


**(a)** **(b)**

**(c)** **(d)**

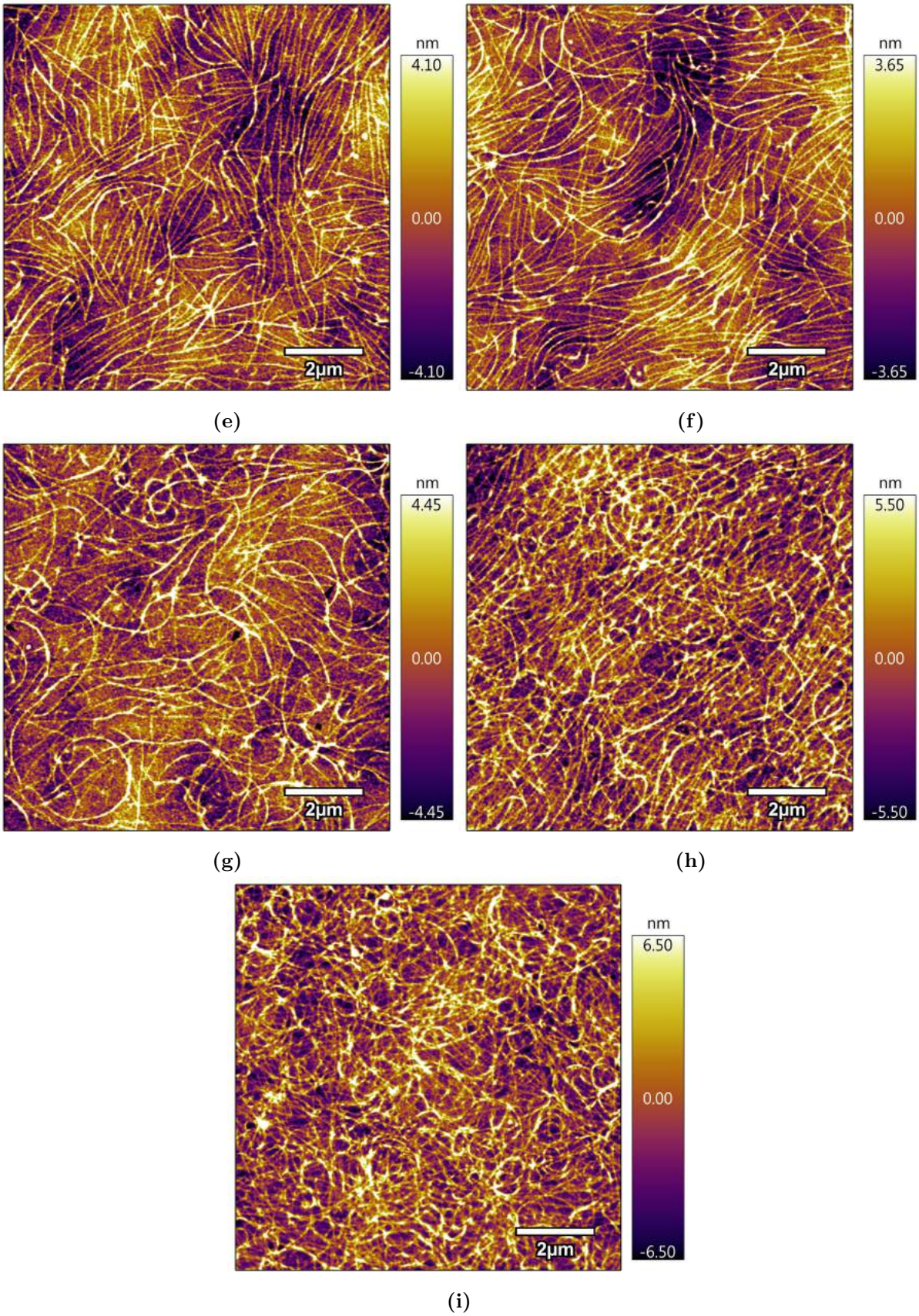


**Figure 4.18:** AFM images of as-cast films that were fabricated from 0.5wt% P3HT solution at (a) 0, (b) 1, (c) 2, (d) 3, (e) 4, (f) 6, (g) 12, (h) 24 and (i) 96 hours.

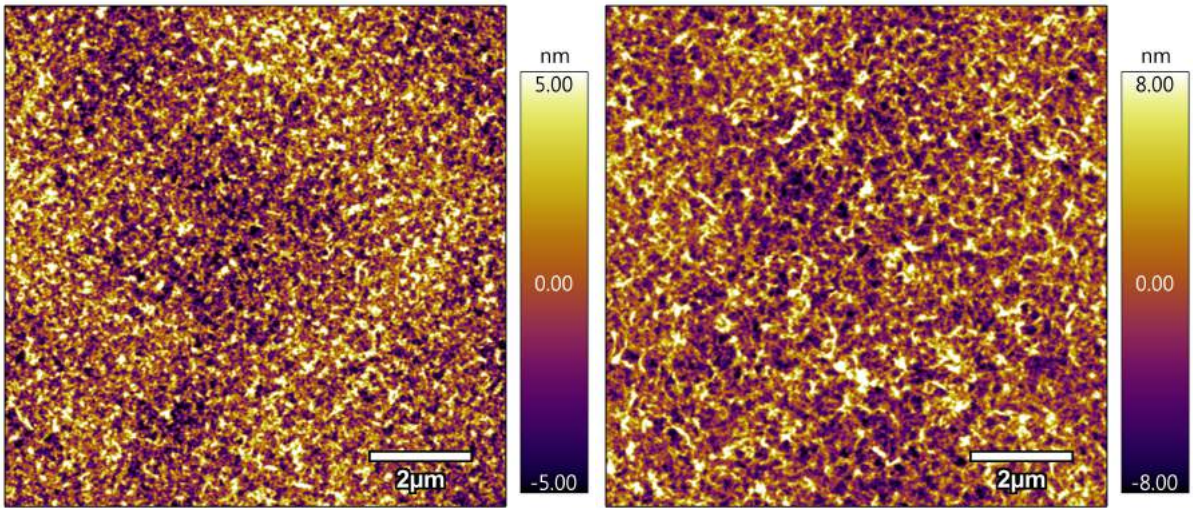
nm
5.00
0.00
-5.00
2µm

**(a)**


nm
8.00
0.00
-8.00
2µm

**(b)**

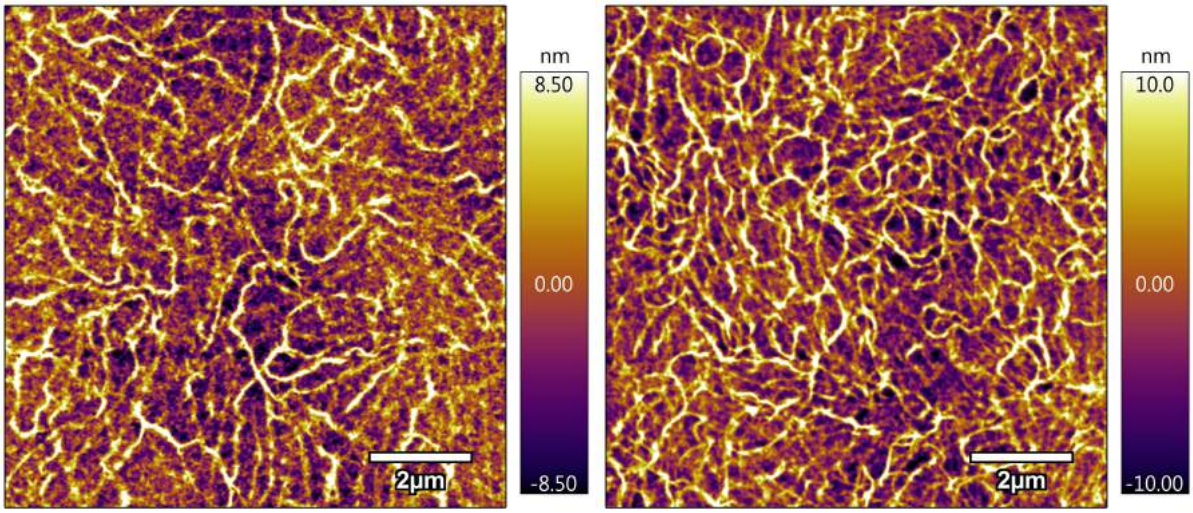
nm
8.50
0.00
-8.50
2µm

**(c)**


nm
10.0
0.00
-10.00
2µm

**(d)**

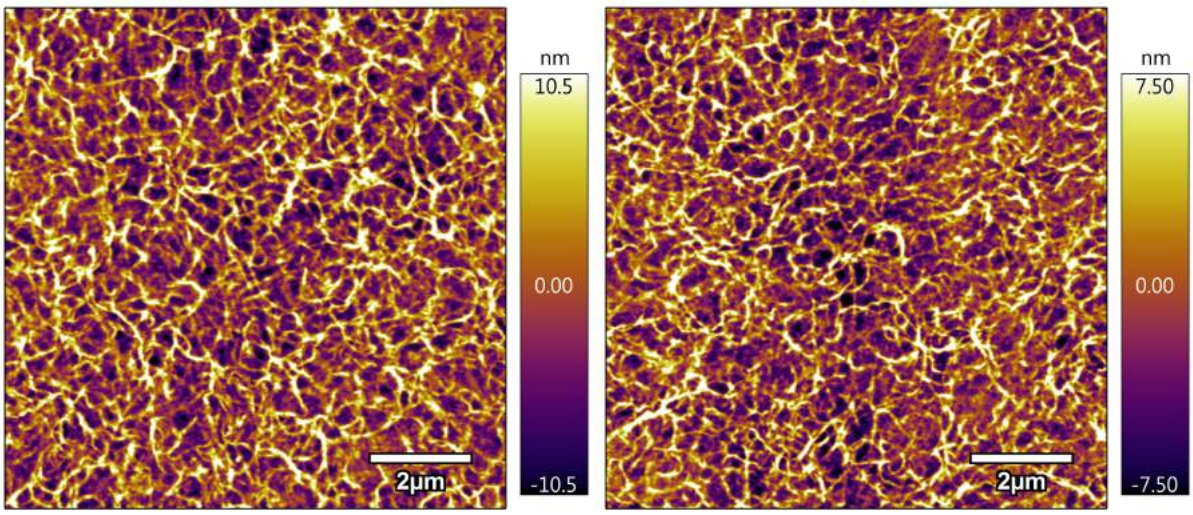
nm
10.5
0.00
-10.5
2µm

**(e)**


nm
7.50
0.00
-7.50
2µm

**(f)**

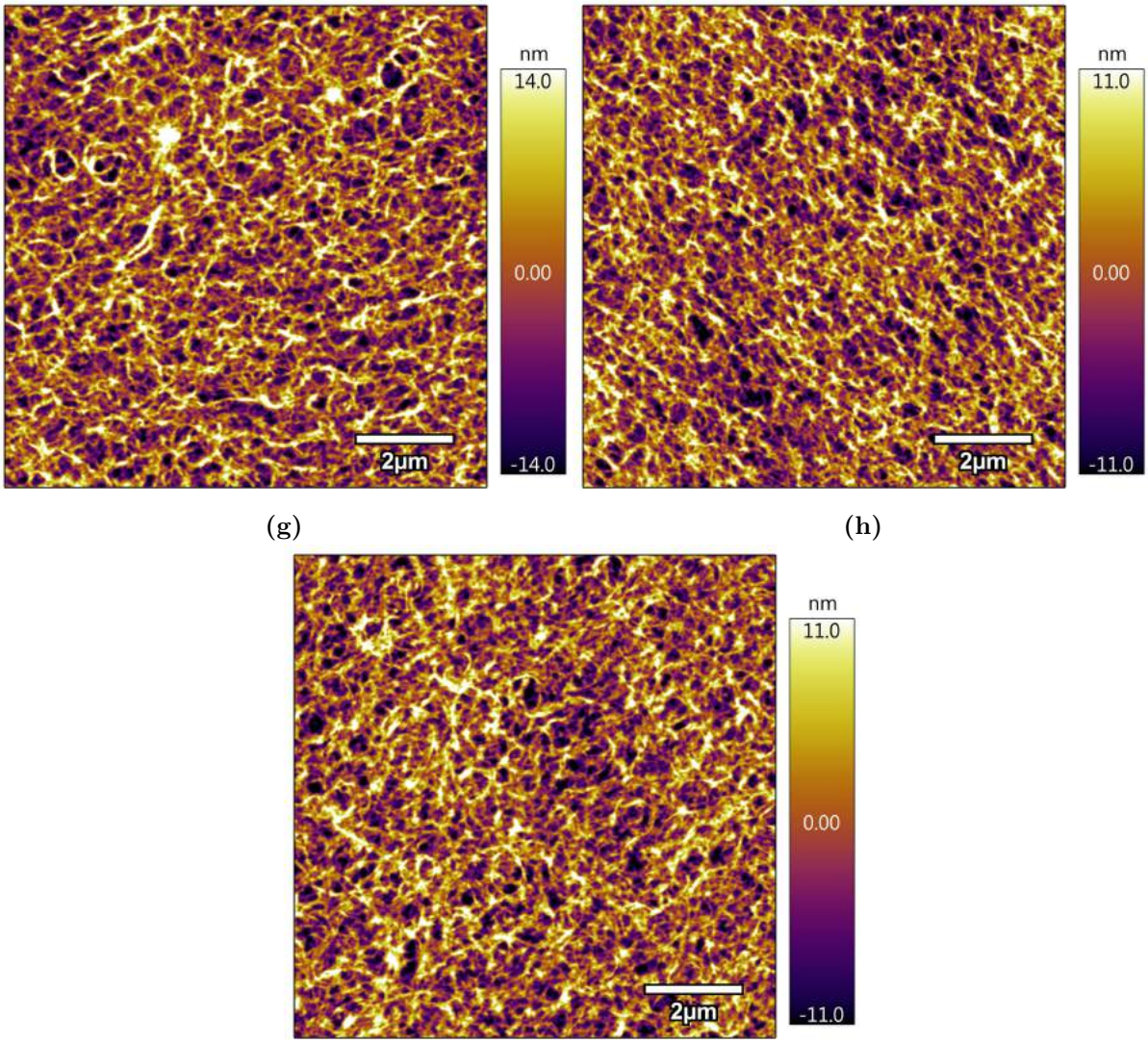


**Figure 4.19:** AFM images of as-cast films that were fabricated from 1.0wt% P3HT solution at (a) 0, (b) 1, (c) 2, (d) 3, (e) 4, (f) 6, (g) 12, (h) 24 and (i) 96 hours.

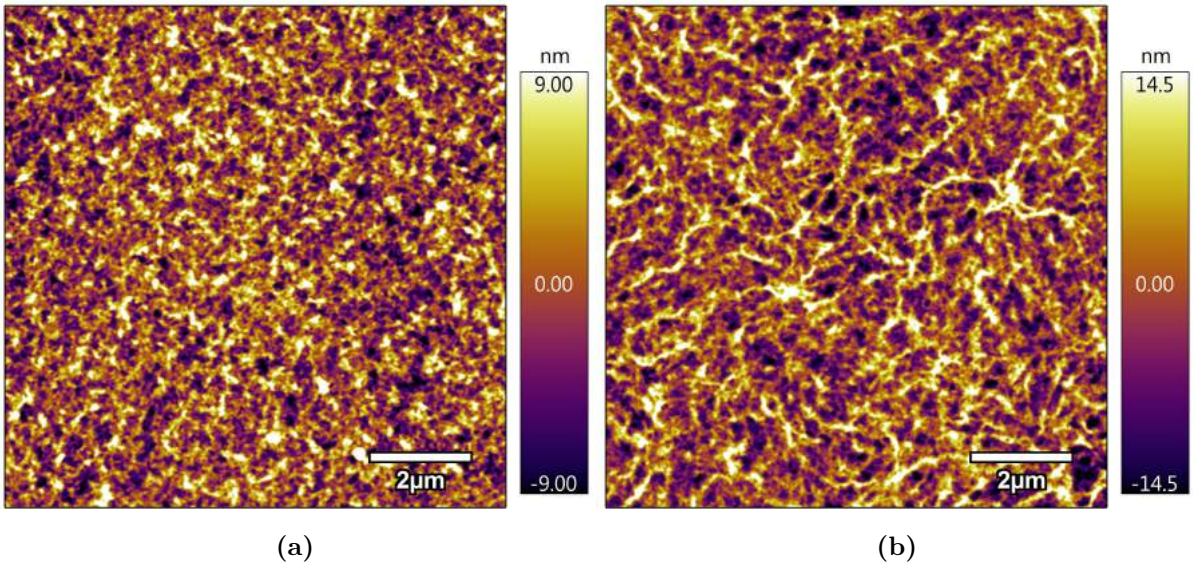

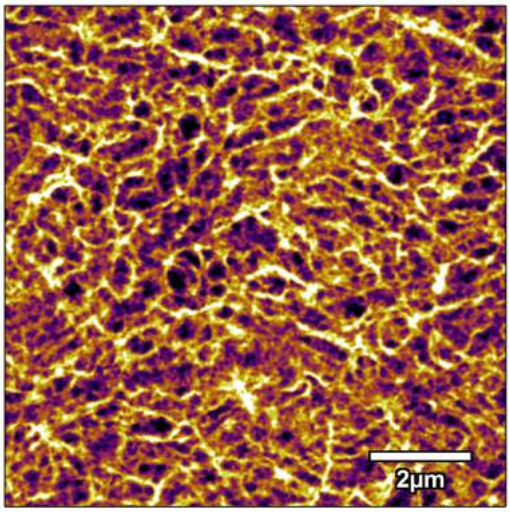
nm
15.0
0.00
-15.0
2µm

**(c)**

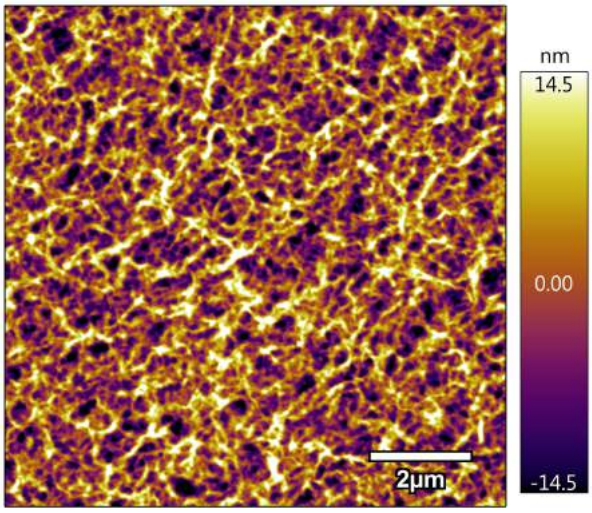
nm
14.5
0.00
-14.5
2µm

**(d)**

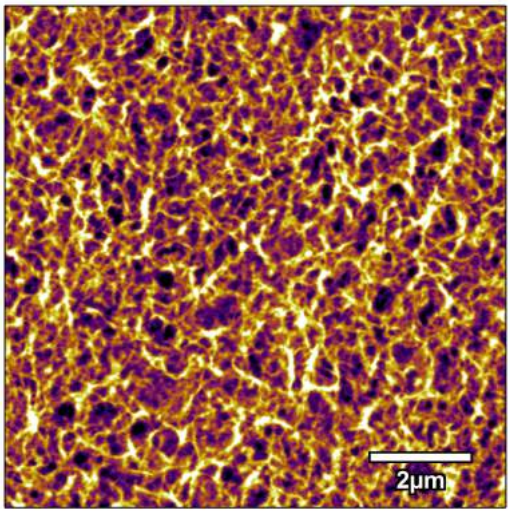
nm
13.5
0.00
-13.5
2µm

**(e)**

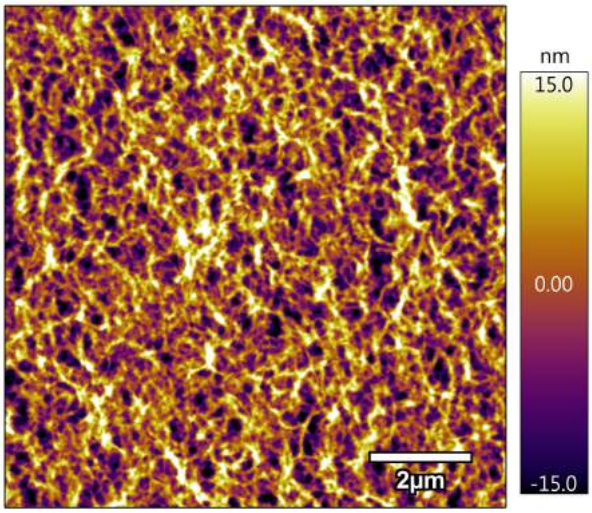
nm
15.0
0.00
-15.0
2µm

**(f)**

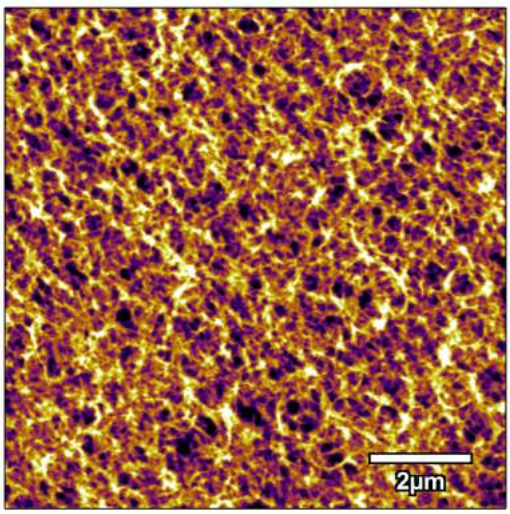
nm
13.0
0.00
-13.0
2µm

**(g)**

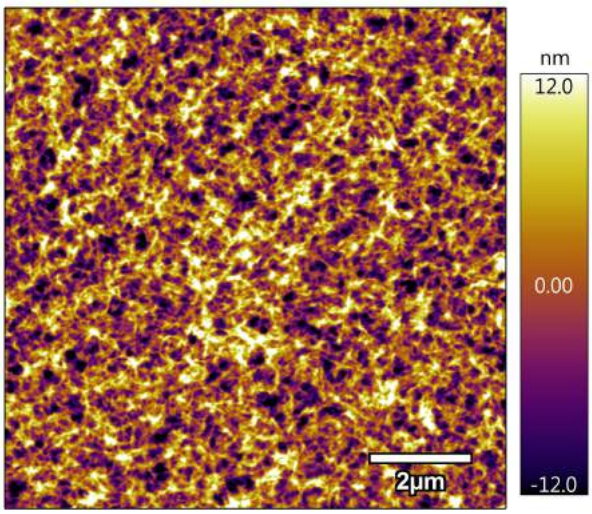
nm
12.0
0.00
-12.0
2µm

**(h)**

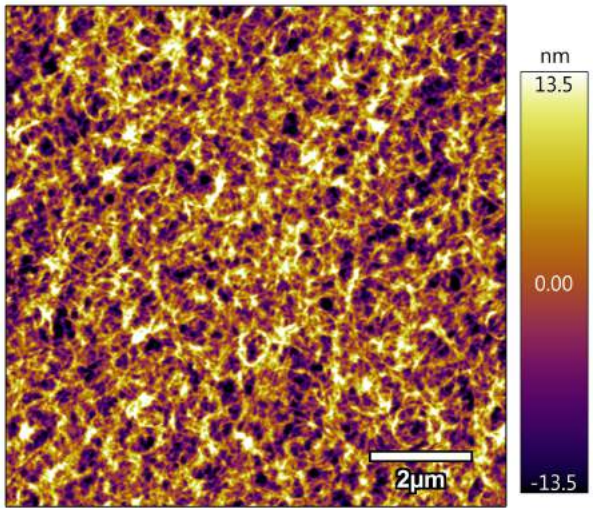


**(i)**

**Figure 4.20:** AFM images of as-cast films that were fabricated from 1.5wt% P3HT solution at (a) 0, (b) 1, (c) 2, (d) 3, (e) 4, (f) 6, (g) 12, (h) 24 and (i) 96 hours.

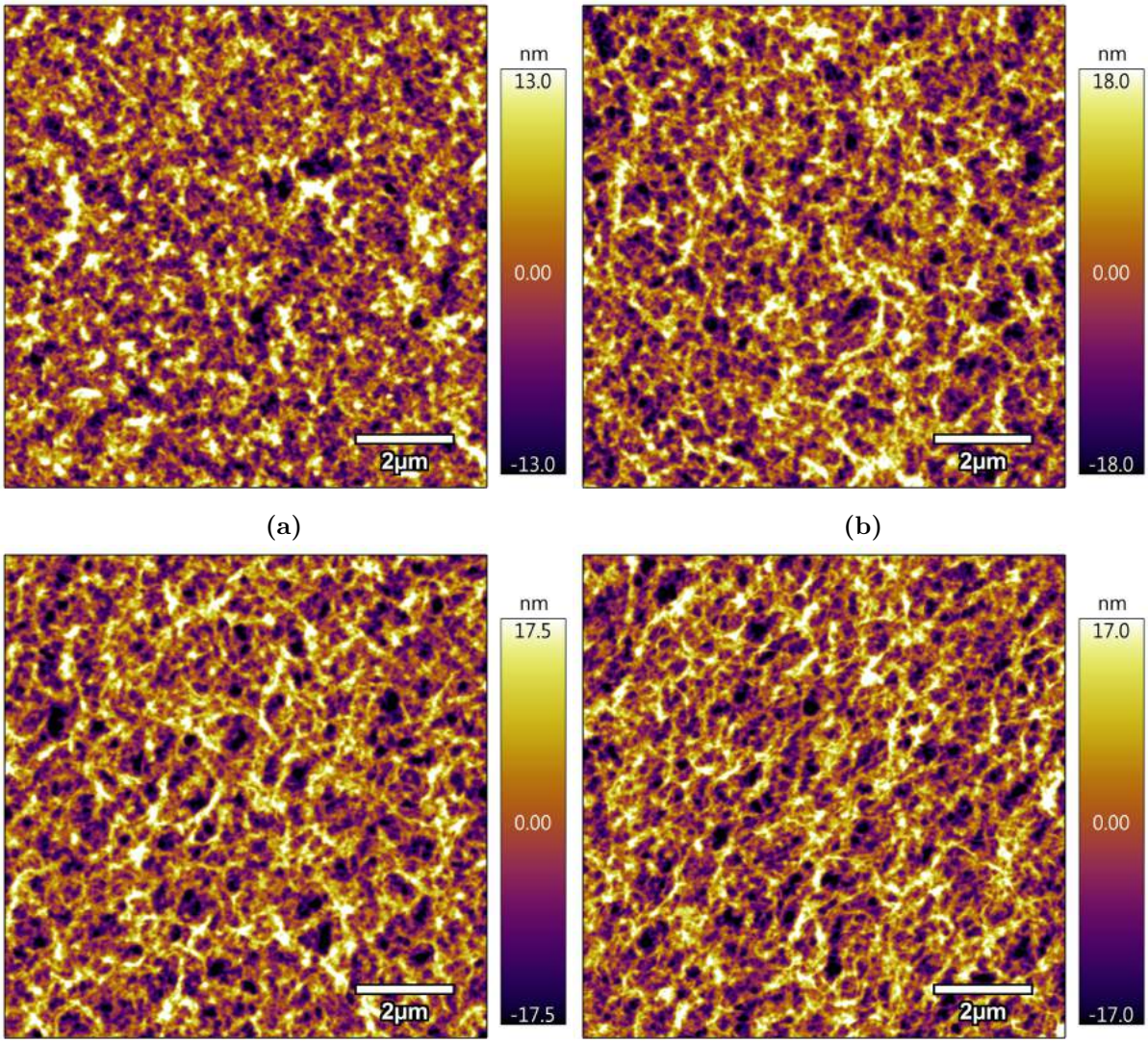


**(a)** **(b)**

**(c)** **(d)**

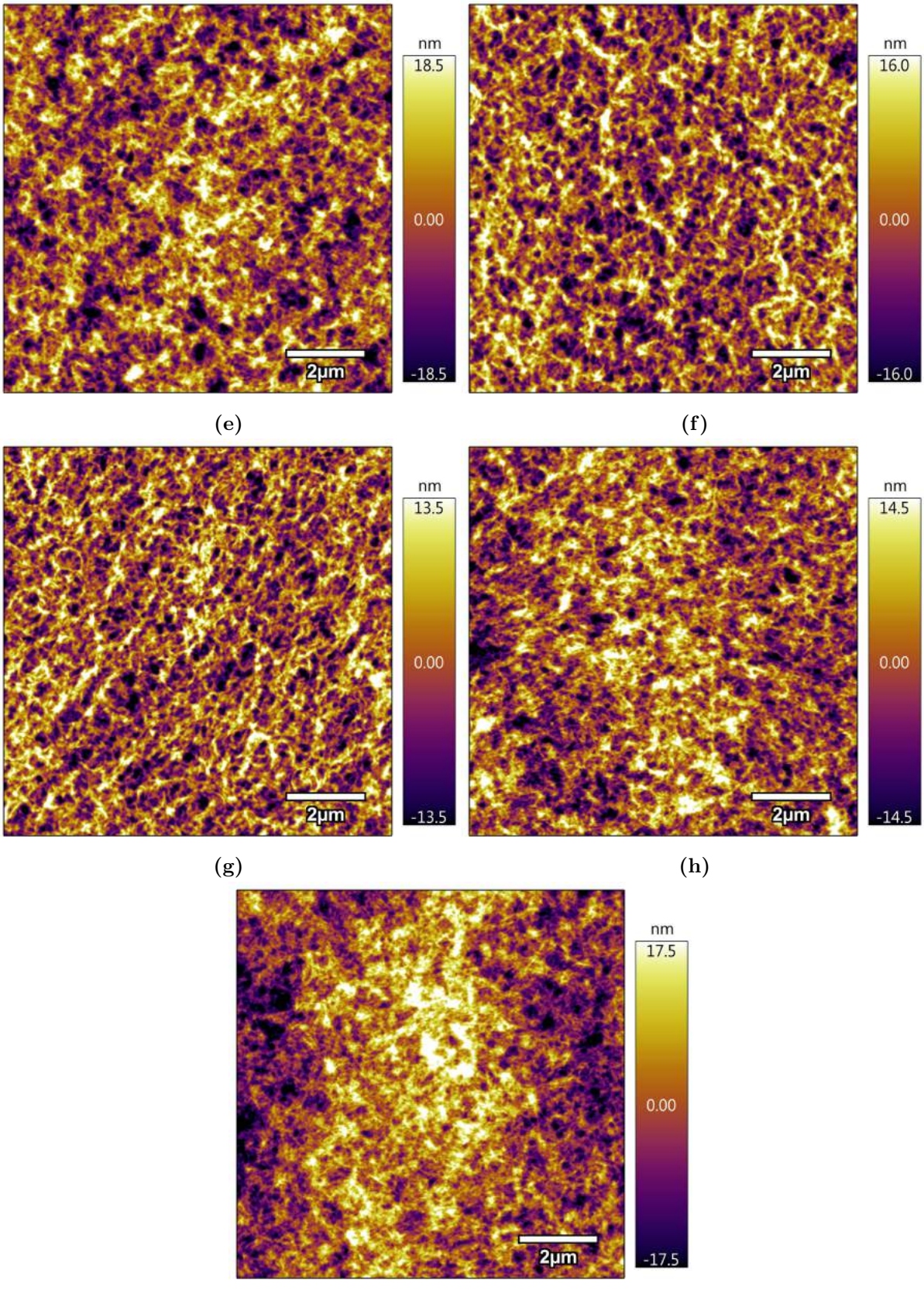


**Figure 4.21:** AFM images of as-cast films that were fabricated from 2.0wt% P3HT solution at (a) 0, (b) 1, (c) 2, (d) 3, (e) 4, (f) 6, (g) 12, (h) 24 and (i) 96 hours.

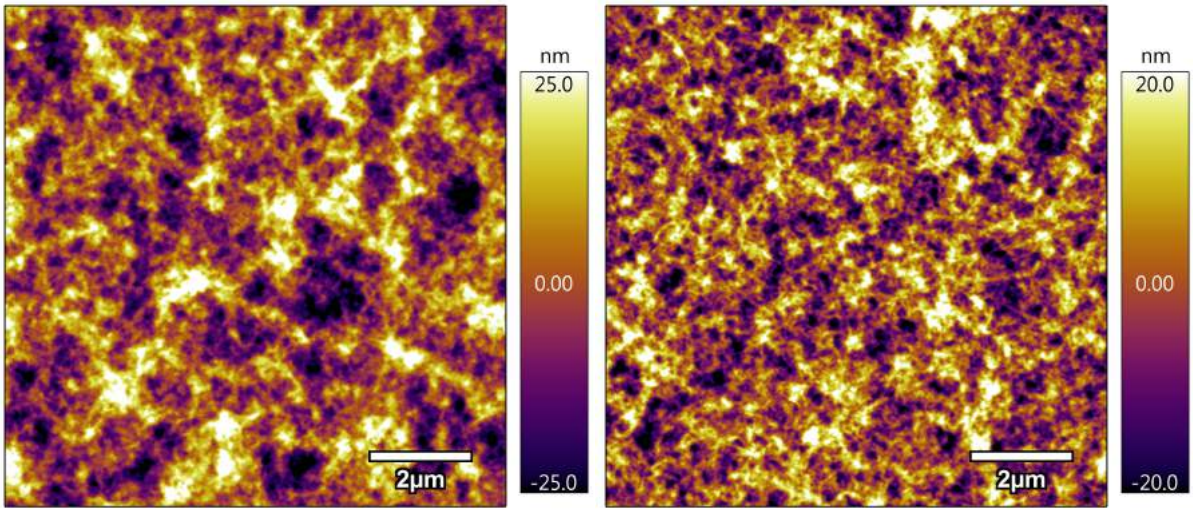
nm
25.0
0.00
-25.0
2μm

**(a)**


nm
20.0
0.00
-20.0
2μm

**(b)**

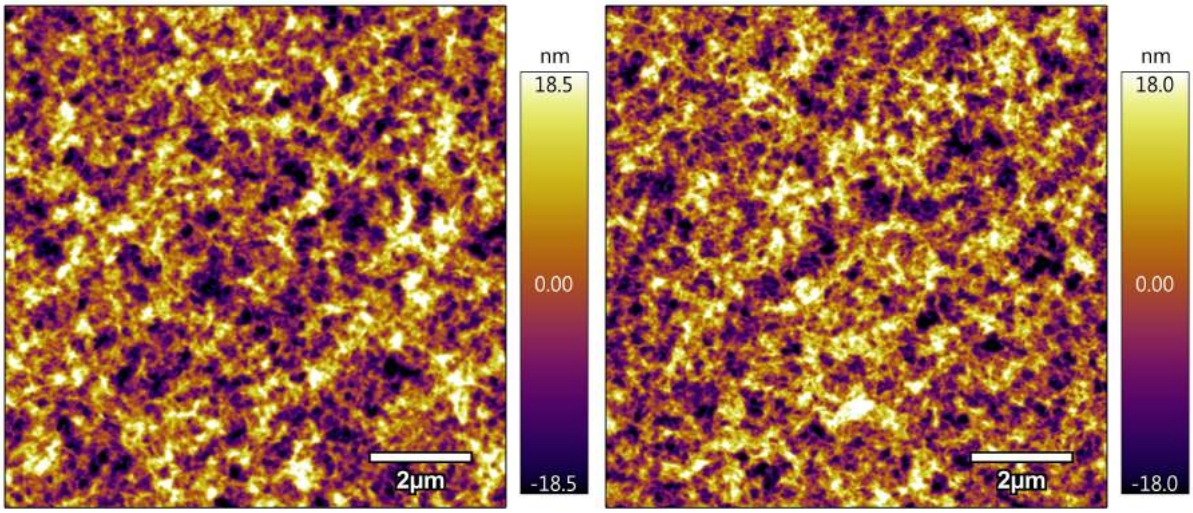
nm
18.5
0.00
-18.5
2μm

**(c)**


nm
18.0
0.00
-18.0
2μm

**(d)**

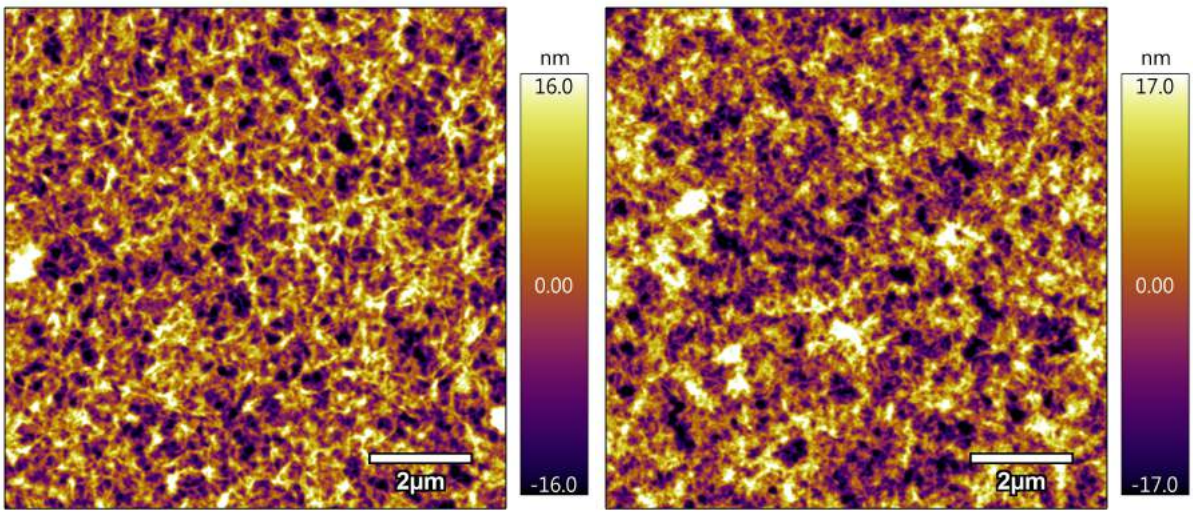
nm
16.0
0.00
-16.0
2μm

**(e)**


nm
17.0
0.00
-17.0
2μm

**(f)**

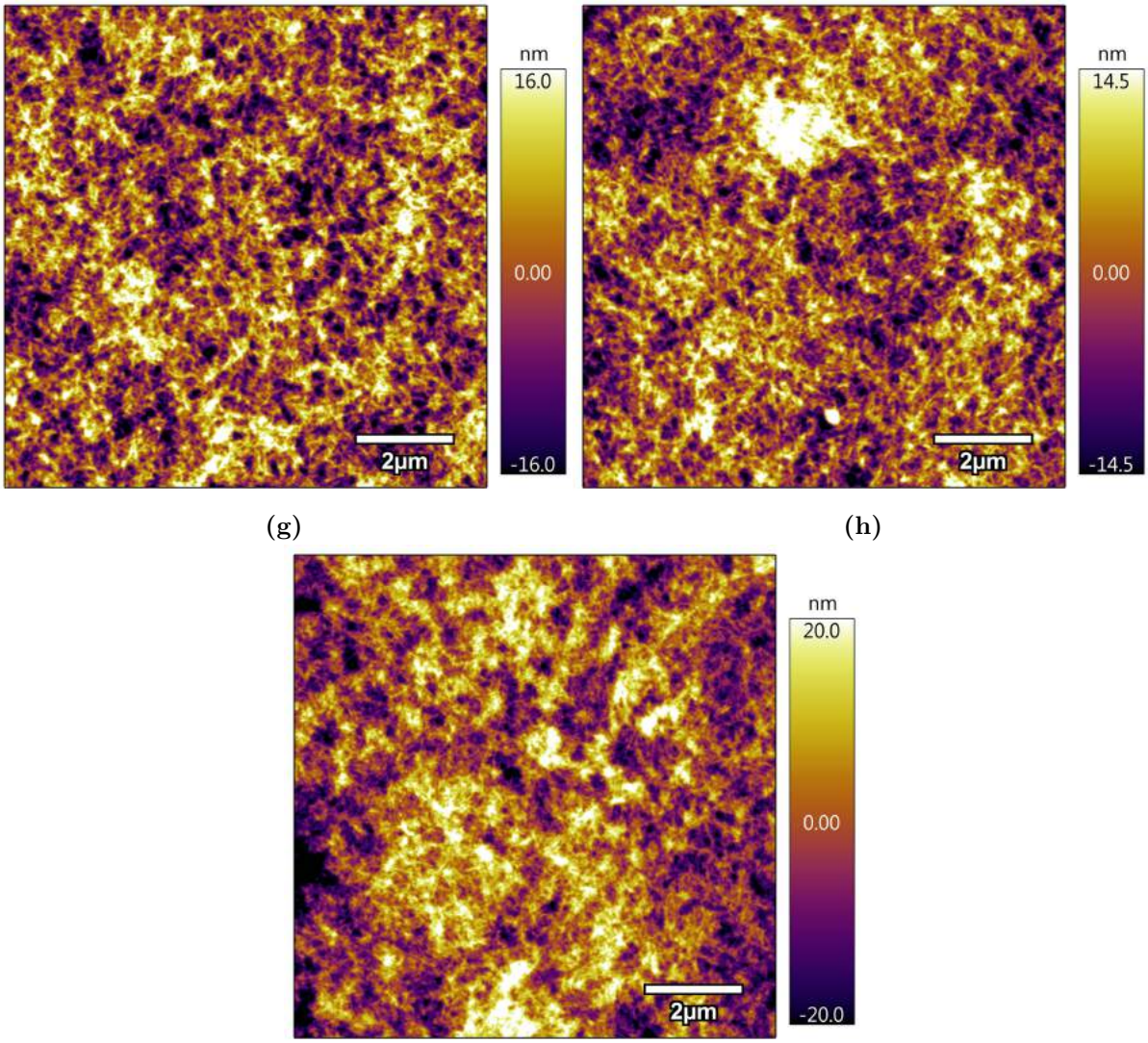


**Figure 4.22:** AFM images of as-cast films that were fabricated from 3.0wt% P3HT solution at (a) 0, (b) 1, (c) 2, (d) 3, (e) 4, (f) 6, (g) 12, (h) 24 and (i) 96 hours.

Upon thermal annealing at 140°C under vacuum atmosphere, the 50-nm thick films which were deposited from the fully aged 1.0 wt% solution formed fractal snowflakes structure all over the film. Although a previous study[106] had observed similar structures in P3HT:PCBM thin films, these structures were identified to be crystalline PCBM and not P3HT. These snowflakes had not been observed before in pure P3HT thin films and likely arose due to the self-assembly of the P3HT fibres during annealing. The topography image (Figure 4.23a) revealed that the snowflakes grew about 12 nm on top of the polymer matrix and were surrounded by regions of P3HT fibres which appeared to be less dense and lower than the overall film. These differences suggested that P3HT in the surrounding regions, fibres and possibly amorphous, diffuses and aggregates to form these dendritic structure. Since the polymer crystallisation in thin films is supressed, Reiter *et al.*[107], through a study of the crystallisation of low molecular-weight polyethyleneoxide (PEO), suggested that the dendritic growth in a polymer thin film crystallisation follows the diffusion-limited aggregation where thicker regions will act

as the nucleation sites and polymer chains, through the Brownian motion, cluster together to form aggregates.

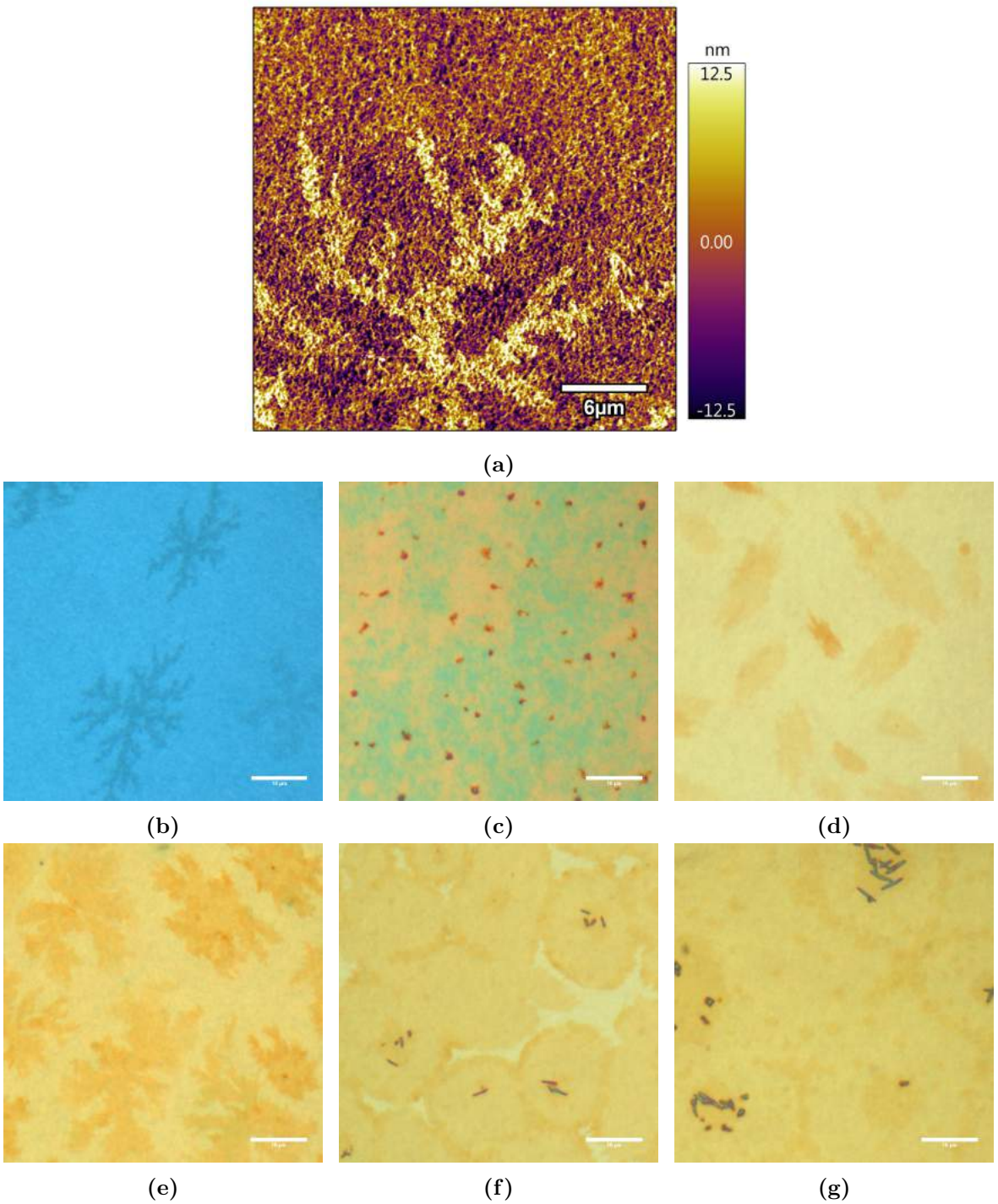


**(a)** **(b)** **(c)** **(d)** **(e)** **(f)** **(g)**

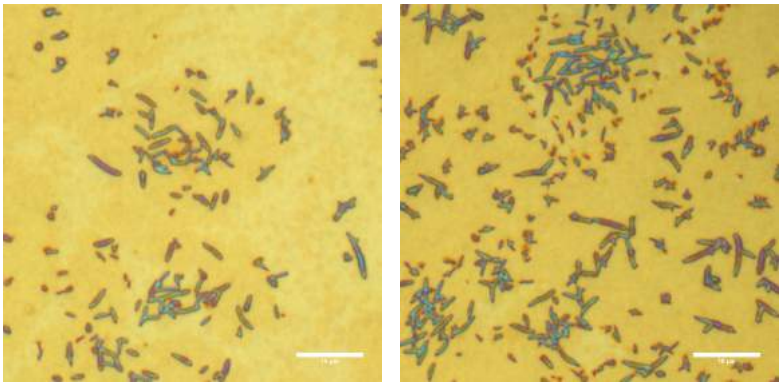

**(h)** **(i)**

**Figure 4.23:** The fractal snowflake crystal that formed in 50-nm thick film upon annealing as seen through (a) AFM and (b) optical microscope. Optical microscope images of (c) 292 nm, (d) 749 nm, (e) 1165 nm, (f) 1493 nm, (g) 1921 nm, (h) 2574 nm and (i) 3490 nm thick films also demonstrate that these fractal snowflakes developed into rod-like structures as film thickness increases. The length of the scale bar is 10 µm.

The formation of snowflake structure was likely to be driven by surface energy. To confirm this hypothesis, P3HT films of different thicknesses were fabricated and thermally annealed. As shown by Figure 4.23b–4.23i, these structures were found to evolve with film thickness, from fractal snowflakes (film thickness: 50 nm) to rod-like structures (film thickness: 3.490 µm). Initially, an increase of film thickness to about 1.165 µm was followed by the growth of the snowflakes. As the film thickness increased further, these snowflakes grew until they overlap one another and rod-like structures started to appear on thicker regions, including the centre of the snowflakes and the overlapping regions. Subsequently, an increase in film thickness only resulted in an increase in the number and size of these polymer rods.

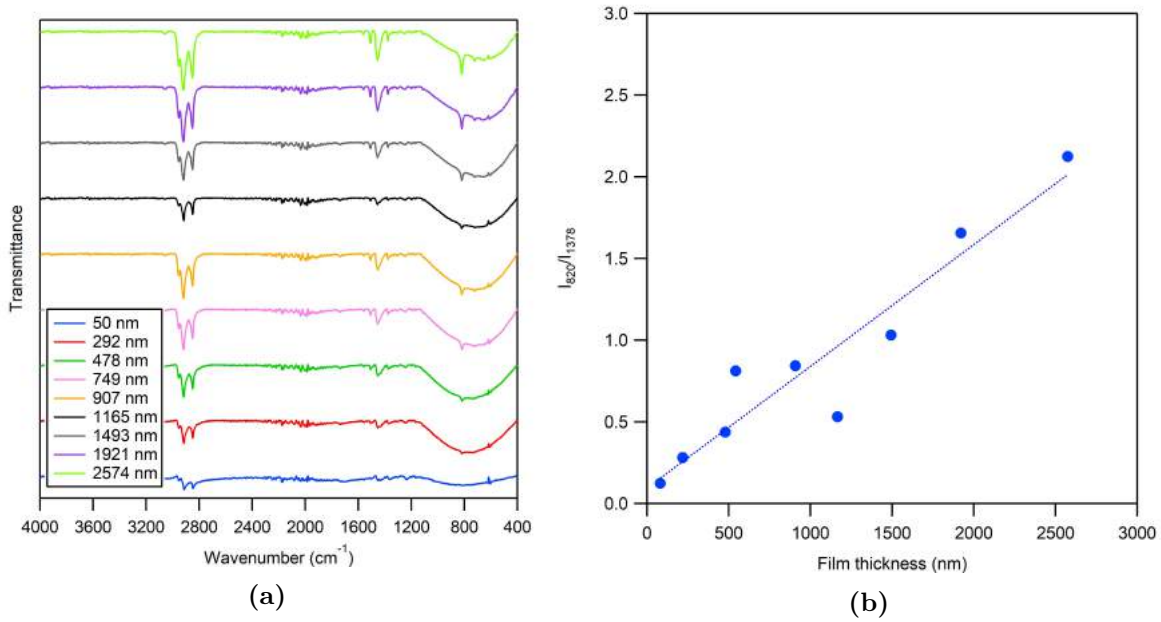


**(a)** **(b)**

**Figure 4.24:** (a) IR reflectance spectrum of annealed aged P3HT films and (b) a plot of the ratio of the out of plane C-H in the thiophene ring peak (∼820 cm-1) to the CH3 deformation peak (∼1378 cm-1) versus film thickness (right). The dotted line in (b) represents a linear fit.

The films were further studied by analysing their IR reflectance spectrum (Figure 4.24a). Taking the ratio of the out of plane C-H in the thiophene ring peak (∼820 cm-1), which is associated with the crystalline structure of the polymer[108], to the CH3 deformation peak (∼1378 cm-1), which was found to be insensitive to any structural change in the film[109], we discovered a linearly increasing trend of that ratio with film thickness (Figure 4.24b). This trend clearly demonstrates that the crystallinity of the polymer in the film is improved with increasing film thickness.

Moreover, the evolution of the film morphology indicates that these structures arose as a result of film confinement in the vertical direction, the interaction between interfaces as well as influenced by the kinetics of solvent evaporation and crystallisation[71]. In thin films, the solvent evaporation is rapid, resulting in a crystallisation kinetic that is constrained by both the crystallisation time and film thickness. In contrast, the rate of solvent evaporation in thick films is slow, providing ample time for the polymer to crystallise and form a more energetically favourable structure without being restricted by the film thickness and the interfacial energy between the substrate and the film. Initial observations suggest that these structures are detrimental to the performance of an organic solar cell as they represent a structure that is analogous to the PCBM aggregates in a P3HT:PCBM film. However, an active layer with these structures could potentially serve a better purpose for other applications, such as transistors.

Unfortunately, we were not able to reproduce the same findings several weeks after the initial observation. We observed the first snowflakes in September, when both the humidity and the temperature were low. The irreproducibility was likely to be the results of the change in season, from winter to summer, which is followed by a rise in humidity and temperature.

# Chapter 5

# Conclusions

We have studied P3HT:PCBM films prepared from chlorobenzene with various compositions and the effects of thermal annealing on structure. As-cast films exhibited homogeneous and smooth surface with a low degree of polymer crystallinity, which was attributed to the edge-on P3HT crystals that formed in solution and during the casting process. Thermally annealing P3HT:PCBM films greatly improves the crystallinity of the polymer without altering the crystal orientation, whilst also induces phase separation as the PCBM molecules, being pushed out during P3HT crystallisation, diffuse through the amorphous fraction of the polymer. The fact that at high PCBM loadings, this phase separation was followed by the aggregation of PCBM molecules to form macroscopic aggregates on the surface of the films, suggests that the fullerene is partially miscible in P3HT and that there are at least three phases that coexist in the film: crystalline P3HT, crystalline PCBM and an intermixed region of P3HT and PCBM.

As revealed by our study of annealing the films at different temperature, the diffusion of PCBM in the polymer matrix is temperature-dependent. At low temperature, there was not any aggregates observed, whereas at high temperature, there is sufficient thermal energy for PCBM to diffuse and form massive 'fans'. We also observed that the nucleation and growth of PCBM aggregates are two competing mechanisms and that they are influenced by both the PCBM loading and the annealing temperature.

Interestingly, it was found that PCBM influences the overall active layer morphology differently at different concentrations regardless whether the films are annealed or not. At low PCBM loadings, it serves as a nucleating agent and enhances P3HT crystallisation, while at high PCBM loadings, it disrupts the ordering of P3HT. Due to this duality of PCBM behaviour in a P3HT:PCBM film, it is crucial to select the optimum PCBM loading at which there is sufficient PCBM to form percolation pathways but not too much that it disturbs the crystallisation of P3HT.

We then proceeded to study solution-grown P3HT fibres as a technique to improve polymer crystallinity without inducing PCBM aggregation. We successfully fabricated P3HT fibres from solutions of different concentrations, ranging from 0.1 to 4.5 wt%, and analysed their growth with UV-Vis and AFM. The nucleation and the rate of growth of P3HT fibres are

strongly influenced by the concentration of the solutions. Consequently, it enables fine-tuning of P3HT crystals morphology through controlling both the concentration and the ageing time of the solution.

Future work will be to investigate how the addition of PCBM and doping affects the nucleation and growth of P3HT fibres in solution, both during and after heat treatment, as well as the morphology and the electrical properties of the active layer.

# Appendix A

# Measurement of mean crystalline domain size from the diffraction pattern

The Scherrer equation:

$$\tau = \frac{K\lambda}{\beta \cos\theta}$$

$\beta$ was calculated by normalising the FWHM with respect to PCBM loading as follow:

$$\beta = \frac{FWHM}{1 - \frac{PCBM\ loading}{100}}$$

| Sample's name | FWHM (°)* | $\beta$ (°) | $2\theta$ (°) | Mean size of P3HT crystalline domains (Å) |
|---|---|---|---|---|
| As-cast 0% PCBM | 0.679 | 0.679 | 5.845 | 117.1 |
| As-cast 10% PCBM | 0.655 | 0.728 | 5.852 | 109.3 |
| As-cast 20% PCBM | 0.593 | 0.741 | 5.860 | 107.3 |
| As-cast 30% PCBM | 0.539 | 0.770 | 5.877 | 103.3 |
| As-cast 40% PCBM | 0.587 | 0.978 | 5.876 | 81.3 |
| As-cast 50% PCBM | 0.620 | 1.240 | 5.873 | 64.1 |
| Annealed 0% PCBM | 0.415 | 0.415 | 5.578 | 191.7 |
| Annealed 10% PCBM | 0.386 | 0.429 | 5.497 | 185.1 |
| Annealed 20% PCBM | 0.386 | 0.482 | 5.478 | 164.8 |
| Annealed 30% PCBM | 0.371 | 0.530 | 5.486 | 150.1 |
| Annealed 40% PCBM | 0.350 | 0.583 | 5.510 | 136.4 |
| Annealed 50% PCBM | 0.460 | 0.919 | 5.876 | 86.6 |

Note:
$K = 0.9$
$\lambda = 1.54$ Å
*The FWHM was obtained by fitting a Lorentzian fit on the (100) peak.

# Bibliography


[1] R. Perez and M. Perez, *The IEA SHC Solar Update*, 2009, **50**, 2–3.

[2] European Photovoltaic Industry Association, *Global market outlook for photovoltaics until 2016*, `http://large.stanford.edu/courses/2012/ph240/vidaurre1/docs/masson.pdf`, 2012.

[3] T. N. Tibbits, P. Beutel, M. Grave, C. Karcher, E. Oliva, G. Siefer, A. Wekkeli, M. Schachtner, F. Dimroth, A. W. Bett *et al.*, Proceedings of the 29th European Photovoltaic Solar Energy Conference and Exhibition, 2014, pp. 1–4.

[4] G. Inzelt, *Conducting polymers: a new era in electrochemistry*, Springer Science & Business Media, 2012.

[5] H. Shirakawa, E. J. Louis, A. G. MacDiarmid, C. K. Chiang and A. J. Heeger, *Journal of the Chemical Society, Chemical Communications*, 1977, 578–580.

[6] C. W. Tang, *Applied Physics Letters*, 1986, **48**, 183–185.

[7] B. M. Illescas and N. Martín, *Comptes Rendus Chimie*, 2006, **9**, 1038–1050.

[8] T. Liu and A. Troisi, *Advanced Materials*, 2013, **25**, 1038–1041.

[9] M. T. Dang, L. Hirsch and G. Wantz, *Advanced Materials*, 2011, **23**, 3597–3602.

[10] S. H. Lee, D. H. Kim, J. H. Kim, G. S. Lee and J. G. Park, *The Journal of Physical Chemistry C*, 2009, **113**, 21915–21920.

[11] S. H. Lee, J. H. Kim, T. H. Shim and J. G. Park, *Electronic Materials Letters*, 2009, **5**, 47–50.

[12] M. C. Scharber and N. S. Sariciftci, *Progress in Polymer Science*, 2013, **38**, 1929–1940.

[13] A. Haugeneder, M. Neges, C. Kallinger, W. Spirkl, U. Lemmer, J. Feldmann, U. Scherf, E. Harth, A. Gügel and K. Müllen, *Physical Review B*, 1999, **59**, 15346–15351.

[14] R. R. Lunt, N. C. Giebink, A. A. Belak, J. B. Benziger and S. R. Forrest, *Journal of Applied Physics*, 2009, **105**, 053711.

[15] G. Yu and A. J. Heeger, *Journal of Applied Physics*, 1995, **78**, 4510–4515.

[16] C. J. Brabec, S. Gowrisanker, J. J. Halls, D. Laird, S. Jia and S. P. Williams, *Advanced Materials*, 2010, **22**, 3839–3856.

[17] C. Deibel and V. Dyakonov, *Reports on Progress in Physics*, 2010, **73**, 096401.

[18] S. P. Economopoulos, G. Itskos, P. A. Koutentis and S. A. Choulis, in *Organic Photovoltaics: Materials, Device Physics, and Manufacturing Technologies*, ed. C. Brabec, U. Scherf and V. Dyakonov, Wiley-VCH, 2014, pp. 1–26.

[19] A. Facchetti, *Materials Today*, 2013, **16**, 123–132.

[20] S. Khodabakhsh, B. M. Sanderson, J. Nelson and T. S. Jones, *Advanced Functional Materials*, 2006, **16**, 95–100.

[21] A. Arias, M. Granström, D. Thomas, K. Petritsch and R. Friend, *Physical Review B*, 1999, **60**, 1854–1860.

[22] F. Zhang, A. Gadisa, O. Inganäs, M. Svensson and M. Andersson, *Applied Physics Letters*, 2004, **84**, 3906–3908.

[23] T. M. Clarke, A. M. Ballantyne, J. Nelson, D. D. Bradley and J. R. Durrant, *Advanced Functional Materials*, 2008, **18**, 4029–4035.

[24] G. Yu, J. Gao, J. C. Hummelen, F. Wudl and A. J. Heeger, *Science*, 1995, **270**, 1789–1791.

[25] K. Kim, J. Liu and D. L. Carroll, *Applied Physics Letters*, 2006, **88**, 181911.

[26] S. H. Park, A. Roy, S. Beaupré, S. Cho, N. Coates, J. S. Moon, D. Moses, M. Leclerc, K. Lee and A. J. Heeger, *Nature Photonics*, 2009, **3**, 297.

[27] P. Schilinsky, C. Waldauf and C. J. Brabec, *Applied Physics Letters*, 2002, **81**, 3885–3887.

[28] B. A. Gregg and M. C. Hanna, *Journal of Applied Physics*, 2003, **93**, 3605–3614.

[29] A. C. Mayer, S. R. Scully, B. E. Hardin, M. W. Rowell and M. D. McGehee, *Materials Today*, 2007, **10**, 28–33.

[30] D. D. Fung and W. C. Choy, in *Organic Solar Cells*, ed. W. C. Choy, Springer, 2013, pp. 1–16.

[31] L. J. Koster, E. Smits, V. Mihailetchi and P. Blom, *Physical Review B*, 2005, **72**, 085205.

[32] K. M. Coakley and M. D. McGehee, *Chemistry of Materials*, 2004, **16**, 4533–4542.

[33] W. C. Tsoi, S. J. Spencer, L. Yang, A. M. Ballantyne, P. G. Nicholson, A. Turnbull, A. G. Shard, C. E. Murphy, D. D. Bradley, J. Nelson *et al.*, *Macromolecules*, 2011, **44**, 2944–2952.

[34] R. D. McCullough, *Advanced Materials*, 1998, **10**, 93–116.

[35] A. Köhler and H. Bässler, *Electronic processes in organic semiconductors: An introduction*, Wiley-VCH, 2015.

[36] B. Kraabel, D. McBranch, N. Sariciftci, D. Moses and A. Heeger, *Physical Review B*, 1994, **50**, 18543–18552.

[37] T. B. Singh, N. Marjanovic, G. Matt, S. Günes, N. Sariciftci, A. M. Ramil, A. Andreev, H. Sitter, R. Schwödiauer and S. Bauer, MRS Online Proceedings Library Archive, 2005, p. I4.9.

[38] A. B. Sieval and J. C. Hummelen, in *Organic Photovoltaics: Materials, Device Physics, and Manufacturing Technologies*, ed. C. Brabec, U. Scherf and V. Dyakonov, Wiley-VCH, 2014, pp. 209–238.

[39] A. Hebard, R. Haddon, R. Fleming and A. Kortan, *Applied Physics Letters*, 1991, **59**, 2109–2111.

[40] V. D. Mihailetchi, J. K. van Duren, P. W. Blom, J. C. Hummelen, R. A. Janssen, J. M. Kroon, M. T. Rispens, W. J. H. Verhees and M. M. Wienk, *Advanced Functional Materials*, 2003, **13**, 43–46.

[41] S. E. Shaheen, C. J. Brabec, N. S. Sariciftci, F. Padinger, T. Fromherz and J. C. Hummelen, *Applied Physics Letters*, 2001, **78**, 841–843.

[42] J. W. Kiel, B. J. Kirby, C. F. Majkrzak, B. B. Maranville and M. E. Mackay, *Soft Matter*, 2010, **6**, 641–646.

[43] A. J. Parnell, A. J. Cadby, O. O. Mykhaylyk, A. D. Dunbar, P. E. Hopkinson, A. M. Donald and R. A. Jones, *Macromolecules*, 2011, **44**, 6503–6508.

[44] P. A. Troshin, H. Hoppe, J. Renz, M. Egginger, J. Y. Mayorova, A. E. Goryachev, A. S. Peregudov, R. N. Lyubovskaya, G. Gobsch, N. S. Sariciftci *et al.*, *Advanced Functional Materials*, 2009, **19**, 779–788.

[45] V. Mihailetchi, J. Wildeman and P. Blom, *Physical Review Letters*, 2005, **94**, 126602.

[46] L. Koster, V. Mihailetchi, H. Xie and P. Blom, *Applied Physics Letters*, 2005, **87**, 203502.

[47] J. Peet, C. Soci, R. Coffin, T. Nguyen, A. Mikhailovsky, D. Moses and G. C. Bazan, *Applied Physics Letters*, 2006, **89**, 252105.

[48] Y. Yao, J. Hou, Z. Xu, G. Li and Y. Yang, *Advanced Functional Materials*, 2008, **18**, 1783–1789.

[49] R. Bechara, N. Leclerc, P. Lévêque, F. Richard, T. Heiser and G. Hadziioannou, *Applied Physics Letters*, 2008, **93**, 246.

[50] N. D. Treat, J. A. N. Malik, O. Reid, L. Yu, C. G. Shuttle, G. Rumbles, C. J. Hawker, M. L. Chabinyc, P. Smith and N. Stingelin, *Nature Materials*, 2013, **12**, 628–633.

[51] S. Berson, R. De Bettignies, S. Bailly and S. Guillerez, *Advanced Functional Materials*, 2007, **17**, 1377–1384.

[52] F. M. McFarland, C. M. Ellis and S. Guo, *The Journal of Physical Chemistry C*, 2017, **121**, 4740–4746.

[53] F. Padinger, R. S. Rittberger and N. S. Sariciftci, *Advanced Functional Materials*, 2003, **13**, 85–88.

[54] M. Berggren, G. Gustafsson, O. Inganäs, M. Andersson, O. Wennerström and T. Hjertberg, *Applied Physics Letters*, 1994, **65**, 1489–1491.

[55] Y. Zhao, Z. Xie, Y. Qu, Y. Geng and L. Wang, *Applied Physics Letters*, 2007, **90**, 043504.

[56] J. H. Park, J. S. Kim, J. H. Lee, W. H. Lee and K. Cho, *The Journal of Physical Chemistry C*, 2009, **113**, 17579–17584.

[57] J. A. Amonoo, E. Glynos, X. C. Chen and P. F. Green, *The Journal of Physical Chemistry C*, 2012, **116**, 20708–20716.

[58] B. Huang, J. A. Amonoo, A. Li, X. C. Chen and P. F. Green, *The Journal of Physical Chemistry C*, 2014, **118**, 3968–3975.

[59] N. D. Treat, C. G. Shuttle, M. F. Toney, C. J. Hawker and M. L. Chabinyc, *Journal of Materials Chemistry*, 2011, **21**, 15224–15231.

[60] K. J. Ihn, J. Moulton and P. Smith, *Journal of Polymer Science Part B: Polymer Physics*, 1993, **31**, 735–742.

[61] W. Ma, C. Yang, X. Gong, K. Lee and A. J. Heeger, *Advanced Functional Materials*, 2005, **15**, 1617–1622.

[62] D. Chirvase, J. Parisi, J. C. Hummelen and V. Dyakonov, *Nanotechnology*, 2004, **15**, 1317.

[63] N. D. Treat, M. A. Brady, G. Smith, M. F. Toney, E. J. Kramer, C. J. Hawker and M. L. Chabinyc, *Advanced Energy Materials*, 2011, **1**, 82–89.

[64] D. E. Motaung, G. F. Malgas, S. S. Nkosi, G. H. Mhlongo, B. W. Mwakikunga, T. Malwela, C. J. Arendse, T. F. Muller and F. R. Cummings, *Journal of Materials Science*, 2013, **48**, 1763–1778.

[65] B. Watts, W. J. Belcher, L. Thomsen, H. Ade and P. C. Dastoor, *Macromolecules*, 2009, **42**, 8392–8397.

[66] D. E. Motaung, G. F. Malgas and C. J. Arendse, *Journal of Materials Science*, 2011, **46**, 4942–4952.

[67] A. L. Ayzner, D. D. Wanger, C. J. Tassone, S. H. Tolbert and B. J. Schwartz, *The Journal of Physical Chemistry C*, 2008, **112**, 18711–18716.

[68] A. Swinnen, I. Haeldermans, J. D'Haen, G. Vanhoyland, S. Aresu, M. D'Olieslaeger, J. Manca *et al.*, *Advanced Functional Materials*, 2006, **16**, 760–765.

[69] S. Schuller, P. Schilinsky, J. Hauch and C. Brabec, *Applied Physics A*, 2004, **79**, 37–40.

[70] C. Müller, T. A. Ferenczi, M. Campoy-Quiles, J. M. Frost, D. D. Bradley, P. Smith, N. Stingelin-Stutzmann and J. Nelson, *Advanced Materials*, 2008, **20**, 3510–3515.

[71] S. van Bavel, E. Sourty, G. de With, K. Frolic and J. Loos, *Macromolecules*, 2009, **42**, 7396–7403.

[72] H. Sirringhaus, N. Tessler and R. H. Friend, *Science*, 1998, **280**, 1741–1744.

[73] J. Liu, M. Arif, J. Zou, S. I. Khondaker and L. Zhai, *Macromolecules*, 2009, **42**, 9390–9393.

[74] L. Li, G. Lu and X. Yang, *Journal of Materials Chemistry*, 2008, **18**, 1984–1990.

[75] A. J. Moulé and K. Meerholz, *Advanced Materials*, 2008, **20**, 240–245.

[76] D. S. Boucher, *Journal of Polymer Science Part B: Polymer Physics*, 2017, **55**, 330–343.

[77] B.-G. Kim, M.-S. Kim and J. Kim, *ACS Nano*, 2010, **4**, 2160–2166.

[78] M. Brinkmann and J.-C. Wittmann, *Advanced Materials*, 2006, **18**, 860–863.

[79] N. Kleinhenz, C. Rosu, S. Chatterjee, M. Chang, K. Nayani, Z. Xue, E. Kim, J. Middlebrooks, P. S. Russo, J. O. Park *et al.*, *Chemistry of Materials*, 2015, **27**, 2687–2694.

[80] B. Schmidt-Hansberg, M. Sanyal, M. F. Klein, M. Pfaff, N. Schnabel, S. Jaiser, A. Vorobiev, E. Muüller, A. Colsmann, P. Scharfer *et al.*, *Acs Nano*, 2011, **5**, 8579–8590.

[81] D. R. Kozub, K. Vakhshouri, L. M. Orme, C. Wang, A. Hexemer and E. D. Gomez, *Macromolecules*, 2011, **44**, 5722–5726.

[82] R. M. Beal, A. Stavrinadis, J. H. Warner, J. M. Smith, H. E. Assender and A. A. Watt, *Macromolecules*, 2010, **43**, 2343–2348.

[83] L. Chang, H. W. Lademann, J.-B. Bonekamp, K. Meerholz and A. J. Moulé, *Advanced Functional Materials*, 2011, **21**, 1779–1787.

[84] W. D. Oosterbaan, V. Vrindts, S. Berson, S. Guillerez, O. Douhéret, B. Ruttens, J. D'Haen, P. Adriaensens, J. Manca, L. Lutsen *et al.*, *Journal of Materials Chemistry*, 2009, **19**, 5424–5435.

[85] F. Machui, S. Langner, X. Zhu, S. Abbott and C. J. Brabec, *Solar Energy Materials and Solar Cells*, 2012, **100**, 138–146.

[86] T. Ameri, J. Min, N. Li, F. Machui, D. Baran, M. Forster, K. J. Schottler, D. Dolfen, U. Scherf and C. J. Brabec, *Advanced Energy Materials*, 2012, **2**, 1198–1202.

[87] G. Li, V. Shrotriya, Y. Yao and Y. Yang, *Journal of Applied Physics*, 2005, **98**, 043704.

[88] B. Tremolet de Villers, C. J. Tassone, S. H. Tolbert and B. J. Schwartz, *The Journal of Physical Chemistry C*, 2009, **113**, 18978–18982.

[89] T. Erb, U. Zhokhavets, G. Gobsch, S. Raleva, B. Stühn, P. Schilinsky, C. Waldauf and C. J. Brabec, *Advanced Functional Materials*, 2005, **15**, 1193–1196.

[90] M. Campoy-Quiles, T. Ferenczi, T. Agostinelli, P. G. Etchegoin, Y. Kim, T. D. Anthopoulos, P. N. Stavrinou, D. D. Bradley and J. Nelson, *Nature Materials*, 2008, **7**, 158.

[91] T. J. Savenije, J. E. Kroeze, X. Yang and J. Loos, *Advanced Functional Materials*, 2005, **15**, 1260–1266.

[92] J. W. Kiel, A. P. Eberle and M. E. Mackay, *Physical Review Letters*, 2010, **105**, 168701.

[93] W. Yin and M. Dadmun, *ACS Nano*, 2011, **5**, 4756–4768.

[94] P. Vanlaeke, A. Swinnen, I. Haeldermans, G. Vanhoyland, T. Aernouts, D. Cheyns, C. Deibel, J. D'Haen, P. Heremans, J. Poortmans *et al.*, *Solar Energy Materials and Solar Cells*, 2006, **90**, 2150–2158.

[95] B. Xue, B. Vaughan, C. H. Poh, K. B. Burke, L. Thomsen, A. Stapleton, X. Zhou, G. W. Bryant, W. Belcher and P. C. Dastoor, *The Journal of Physical Chemistry C*, 2010, **114**, 15797–15805.

[96] P. Karagiannidis, S. Kassavetis, C. Pitsalidis and S. Logothetidis, *Thin Solid Films*, 2011, **519**, 4105–4109.

[97] G. A. Berriman, N. P. Holmes, J. L. Holdsworth, X. Zhou, W. J. Belcher and P. C. Dastoor, *Organic Electronics*, 2016, **30**, 12–17.

[98] Z. Xu, L. M. Chen, G. Yang, C. H. Huang, J. Hou, Y. Wu, G. Li, C. S. Hsu and Y. Yang, *Advanced Functional Materials*, 2009, **19**, 1227–1234.

[99] G. A. Berriman, J. L. Holdsworth, X. Zhou, W. J. Belcher and P. C. Dastoor, *Organic Electronics*, 2016, **38**, 15–20.

[100] F. C. Spano, *The Journal of Chemical Physics*, 2005, **122**, 234701.

[101] F. C. Spano and C. Silva, *Annual Review of Physical Chemistry*, 2014, **65**, 477–500.

[102] E. J. Mittemeijer, in *Fundamentals of Materials Science*, Springer, 2010, pp. 371–461.

[103] S. Hu, *M.Sc. thesis*, University of Tennessee, Knoxville, 2013.

[104] J. Clark, J. F. Chang, F. C. Spano, R. H. Friend and C. Silva, *Applied Physics Letters*, 2009, **94**, 117.

[105] C. Scharsich, R. H. Lohwasser, M. Sommer, U. Asawapirom, U. Scherf, M. Thelakkat, D. Neher and A. Köhler, *Journal of Polymer Science Part B: Polymer Physics*, 2012, **50**, 442–453.

[106] O. Akogwu, W. Akande, T. Tong and W. Soboyejo, *Journal of Applied Physics*, 2011, **110**, 103517.

[107] G. Reiter, G. Castelein and J. U. Sommer, in *Polymer Crystallization*, ed. G. Reiter and J. U. Sommer, Springer, 2003, pp. 131–152.

[108] K. Yazawa, Y. Inoue, T. Yamamoto and N. Asakawa, *Physical Review B*, 2006, **74**, 094204.

[109] G. Zerbi, B. Chierichetti and O. Ingänas, *The Journal of Chemical Physics*, 1991, **94**, 4646–4658.